

Physics-informed data-driven inference of an interpretable equivariant LES model of incompressible fluid turbulence

Matteo Ugliotti^{1†}, Brandon Choi^{1†}, Mateo Reynoso¹, Daniel R. Gurevich², and Roman O. Grigoriev^{1‡}

¹School of Physics, Georgia Institute of Technology, Atlanta, GA 30332, USA

²Department of Mathematics, University of California, Los Angeles, CA 90095, USA

(Received xx; revised xx; accepted xx)

Restrictive phenomenological assumptions represent a major roadblock for the development of accurate subgrid-scale models of fluid turbulence. Specifically, these assumptions limit a model's ability to describe key quantities of interest, such as local fluxes of energy and enstrophy, in the presence of diverse coherent structures. This paper introduces a symbolic data-driven subgrid-scale model that requires no phenomenological assumptions and has no adjustable parameters, yet it outperforms leading LES models. A combination of *a priori* and *a posteriori* benchmarks shows that the model produces accurate predictions of various quantities including local fluxes across a broad range of two-dimensional turbulent flows. While the model is inferred using LES-style spatial coarse-graining, its structure is more similar to RANS models, as it employs an additional field to describe subgrid scales. We find that this field must have a rank-two tensor structure in order to correctly represent both the components of the subgrid-scale stress tensor and the various fluxes.

Key words:

1. Introduction

The objective of large eddy simulations (LES) is to provide an accurate and general description of the evolution of turbulent fluid flows at high Reynolds numbers when the cost of direct numerical simulation becomes prohibitive. Rather than explicitly resolving the computationally small (unresolved) scales, LES represents their effect on the large (resolved) scales through a closure term in the momentum equation, expressed in terms of the subgrid-scale (SGS) stress tensor τ_{ij} . In the most common LES formulations, this tensor is assumed to depend only on the resolved variables, e.g., the filtered velocity $\bar{\mathbf{u}}$, thereby strongly constraining the admissible structure of phenomenological closures. An example of this is the restrictive Boussinesq assumption, which posits a linear relation between these tensors, $\tau_{(ij)} = 2\nu_e \nabla_{(i} \bar{u}_{j)}$, where ν_e is the scalar eddy viscosity and parentheses denote the trace-free symmetric component of a rank-2 tensor.

Within this framework, phenomenological SGS models can be broadly classified into functional, structural, and hybrid approaches. Functional models mainly aim to introduce a statistically appropriate amount of energy dissipation. Indeed, this is the key role of the SGS stress tensor, as turbulent transport typically induces energy transfer towards smaller scales on the net. Prominent

† These authors contributed equally and share first authorship.

‡ Email address for correspondence: roman.grigoriev@physics.gatech.edu

examples of functional models include the Smagorinsky model (Smagorinsky 1963) and its dynamic version (Lilly 1992; Germano *et al.* 1991), both of which rely on the Boussinesq assumption. In contrast, structural models seek to reproduce the SGS stress tensor itself by using a formal series expansion or scaling arguments. Representative examples include the nonlinear/gradient model (NGM) (Leonard 1975; Clark *et al.* 1979a) and the similarity model (Bardina *et al.* 1980). Hybrid approaches combine elements of both classes and include models such as the dynamic nonlinear mixed model (Vreman *et al.* 1996) and the dynamic mixed model (Bardina *et al.* 1980).

Current phenomenological SGS models mostly rely on restrictive physical assumptions such as homogeneity, isotropy, and scale invariance. These are frequently violated, for instance in flows dominated by pronounced coherent structures, where such models become inaccurate even in describing basic properties such as energy dissipation (Moser *et al.* 2021). Even when these assumptions appear to be approximately satisfied, phenomenological models often fail to capture the correct interscale energy transfer, in particular energy fluxes from small to large scales—commonly referred to as backscatter (Vreman *et al.* 1997)—which can be dynamically significant for some types of turbulent flows.

Recent progress in machine learning (ML) has enabled discovery of explicit parameterizations of the closure term using data generated by direct numerical simulations (DNS). The most common approach is based on the application of the Cayley–Hamilton theorem to express the tensor τ_{ij} as a finite sum of linearly independent tensor basis functions, with coefficients given by scalar functions of a finite number of invariants of the strain rate tensor $\nabla_i \bar{u}_j$ (Pope 1975). While this representation is formally complete, inferring the functional form of each coefficient for all of the invariants is extremely challenging. Consequently, practical implementations typically rely on truncating the expansion or restricting the number of invariants retained. Examples include sparse regression approaches such as random forest regression (Ling *et al.* 2016) and sequential thresholding ridge regression (Schmelzer *et al.* 2018), and symbolic regression methods based on genetic expression programming (GEP) (Weatheritt & Sandberg 2017; Reissmann *et al.* 2021).

Sparse regression has also been used to learn the explicit functional form of the closure term, component by component, in terms of the derivatives of the resolved fields but without relying on the Cayley–Hamilton theorem. For instance, relevance vector machines (RVM) have been used to infer a quadratic parameterization resembling NGM for oceanic flows (Zanna & Bolton 2020a) and two-dimensional turbulence (Jakhar *et al.* 2024). A hybrid sparse/symbolic regression algorithm was employed to identify a (scalar) closure in a two-layer model of quasi-geostrophic turbulence (Ross *et al.* 2023) which involves higher-order derivatives of the large-scale variables (here, velocity and potential vorticity). However, none of these approaches ensure that the inferred closure transforms correctly under rotations or yields stable evolution (Jakhar *et al.* 2024).

The bulk of ML studies use deep learning (DL) to yield an implicit, neural network-based parameterization. Representative examples include closures for the momentum equation in two-dimensional (Maulik *et al.* 2019; Kochkov *et al.* 2021) and three-dimensional turbulence (Beck *et al.* 2019), the baroclinic quasi-geostrophic potential vorticity equation (Bolton & Zanna 2019), the advection-diffusion equation driven by isotropic homogeneous turbulent flow (Frezat *et al.* 2021), and the momentum equation in MHD turbulence (Karpov *et al.* 2022). Physical constraints such as symmetries can be incorporated into DL parameterizations through hard or soft constraints, leading to improved performance (Frezat *et al.* 2021; Guan *et al.* 2023; Pawar *et al.* 2023). While DL-based approaches rely on less stringent assumptions, e.g., that the closure can be expressed solely in terms of the resolved variables, resulting parameterizations lack interpretability and have poor generalizability. Moreover, while DL parameterizations tend to reproduce the statistics well, they generally do not improve short-term predictions (Ross *et al.* 2023) and are commonly unstable (Guan *et al.* 2022; Ross *et al.* 2023; Pedersen *et al.* 2023).

It should be emphasized that all the modeling approaches described above do not explicitly

describe subgrid scales and fail to properly capture local fluxes, including backscatter. In this paper, we demonstrate that these two features are fundamentally connected. We draw upon both first-principles analysis and the cutting-edge, data-driven SPIDER framework (Gurevich *et al.* 2024a) to build a interpretable, equivariant, stable and *accurate* subgrid model. The model is inferred and validated in the context of two-dimensional turbulence, a setting characterized by prominent coherent structures and pronounced local fluxes in both directions. The paper is organized as follows. Section 2 introduces our methodology. The results are presented in Section 3. The relation between the structures of the inferred model and existing phenomenological models is discussed in Section 4. Finally, our conclusions are presented in Section 5.

2. Methods

2.1. Governing Equations and Coarse-Graining

In this study, we consider incompressible flows of Newtonian fluids described by the Navier-Stokes equation and divergence-free condition

$$\partial_t u_i + u_j \nabla_j u_i = -\rho^{-1} \nabla_i p + \nu \nabla^2 u_i - \gamma u_i + f_i, \quad (2.1a)$$

$$\nabla_i u_i = 0, \quad (2.1b)$$

where ρ is the density, ν is the kinematic viscosity, γ is the Rayleigh friction coefficient, f_i is the forcing, and the Einstein implicit summation notation is used. We focus exclusively on two-dimensional turbulence which features pronounced coherent structures and significant backscatter, making it an ideal testing ground for the development and validation of SGS models. Since we are primarily interested in modeling turbulence far from any boundaries, we consider flows on a two-dimensional domain Ω of size $\ell_d \times \ell_d$ with periodic boundary conditions (with $\ell_d = 2\pi$).

Our training data was generated from DNS using initial conditions representative of three characteristic regimes of two-dimensional turbulence: forced, statistically stationary turbulence with direct and inverse cascade, and transient freely decaying turbulence. The corresponding vorticity fields are shown in Figure 1 and feature coherent structures (vortices and vorticity filaments) with a characteristic length scale $\ell_i < \ell_d$ to be defined later. For each of the three initial conditions, the flow was evolved for $O(1)$ eddy turnover time (here and below defined as $T_e = 1/\omega_{rms}$ computed using the initial condition) without forcing or Rayleigh friction and with the kinematic viscosity equal to 10^{-4} , 10^{-5} , and 10^{-6} . For the lowest value of viscosity, the corresponding Reynolds numbers $Re = \ell_d u_{rms}/\nu$ are approximately 3×10^5 , 2×10^5 , and 3×10^6 , for flows F1-F3 respectively. Fully-resolved numerical solutions describing these flows were obtained using a pseudospectral solver with 2/3 dealiasing on grids of size 2048^2 , 4096^2 , and 4096^2 , respectively. Additional details on our DNS are given in Appendix A.1.

Our subgrid-scale model was constructed using filtered DNS (FDNS) data, with the filter scales Δ chosen to lie between the fine grid resolution and the size ℓ_i . We define the filter operator, acting on any tensor field ϕ

$$\bar{\phi}(\mathbf{x}) \equiv \int G(|\mathbf{x} - \mathbf{x}'|/\Delta) \phi(\mathbf{x}') d\mathbf{x}', \quad (2.2)$$

where the kernel G has width Δ . Filtered variables are assumed to be resolved on a coarse grid, unlike the fluctuations $\phi' \equiv \phi - \bar{\phi}$. The kernel G should satisfy a number of properties, primarily locality in both real and spectral space, as to minimize the Gibbs phenomenon; the popular Gaussian kernel serves this purpose well (Pope 2000; Sagaut & Meneveau 2006; Vreman *et al.* 1994). We further project the filtered field onto the coarse grid – an operation mathematically equivalent to filtering again with a sharp spectral filter. This additional projection is necessary for data-driven discovery of accurate SGS models in the form of partial differential equations (PDEs), as the grid resolution strongly impacts spatial derivatives.

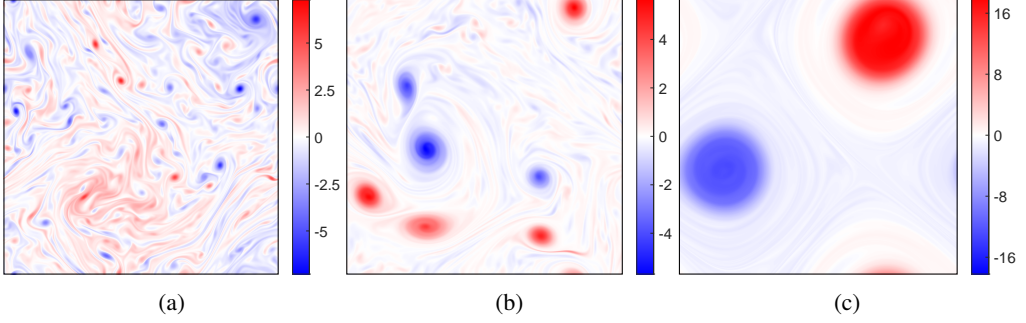


Figure 1: Initial conditions for the three flows F1 (a), F2 (b), and F3 (c). The characteristic integral scale is, respectively, $\ell_i \approx \ell_d/30$, $\ell_d/4$, and $\ell_d/2$.

Applying the combined filtering operator to the system of equations (2.1) yields the governing equation for the filtered (resolved) velocity and pressure fields

$$\partial_t \bar{u}_i + \bar{u}_j \nabla_j \bar{u}_i = -\rho^{-1} \nabla_i \bar{p} + \nu \nabla^2 \bar{u}_i - \gamma \bar{u}_i + \bar{f}_i - \nabla_j \tau_{ij}, \quad (2.3a)$$

$$\nabla_i \bar{u}_i = 0. \quad (2.3b)$$

The closure term $\nabla_j \tau_{ij}$ is written in terms of the subgrid stress tensor $\tau_{ij} \equiv \overline{u_i u_j} - \bar{u}_i \bar{u}_j$. Note that the pure Gaussian filter is invertible, so \mathbf{u} (and therefore τ) can in principle be expressed in terms of $\bar{\mathbf{u}}$ alone in the continuum limit. However, on a discrete grid, the invertibility is lost and so there is no reason to expect that τ can be expressed solely in terms of the resolved variables, as is commonly assumed.

2.2. SGS Stress Tensor Decomposition and Moment Expansion

The loss of information associated with using a coarse grid must be compensated for by introducing new variable(s) that describe subgrid-scales. In order to identify the proper SGS variables, it is fruitful to consider the LCR decomposition of τ (Clark *et al.* 1979b; Germano 1986), into three Galilean invariant components L , C , and R , given by

$$\tau_{ij} = L_{ij} + C_{ij} + R_{ij} \quad (2.4a)$$

$$L_{ij} = \overline{\bar{u}_i \bar{u}_j} - \bar{\bar{u}}_i \bar{\bar{u}}_j \quad (2.4b)$$

$$C_{ij} = \overline{\bar{u}_i u'_j} + \overline{u'_i \bar{u}_j} - \bar{\bar{u}}_i \bar{u}'_j - \bar{u}'_i \bar{\bar{u}}_j \quad (2.4c)$$

$$R_{ij} = \overline{u'_i u'_j} - \overline{u'_i u'_j} \quad (2.4d)$$

The Leonards tensor L encodes large-large scale interactions, the Cross tensor C encodes large-small scale interactions, and the Reynolds tensor R encodes the small-small scale interactions. For invertible filters, it is possible to represent L , C , and R as a function of the resolved velocity $\bar{\mathbf{u}}$ using the moment expansion. For a spatially homogeneous and isotropic filter with finite moments (as is the one adopted in this paper), the filtering operator (2.2) can be written in terms of the gradient operator (Sagaut & Meneveau 2006)

$$\bar{\phi} = \left(1 + \frac{1}{2} \Sigma_{ij}^{(1)} \nabla_i \nabla_j + \frac{1}{24} \Sigma_{ijkl}^{(2)} \nabla_i \nabla_j \nabla_k \nabla_l + \dots \right) \phi \quad (2.5)$$

where $\Sigma^{(n)} = O(\Delta^{2n})$ are tensor coefficients determined by the moments of the filter kernel G . Note that the right-hand-side of Equation (2.5) is a power series in $\delta \equiv \Delta/\ell_i$, where ℓ_i is the characteristic length scale of the flow, with subsequent terms providing progressively smaller

corrections for $\delta \ll 1$. This series can be inverted to express ϕ in terms of $\bar{\phi}$. For a Gaussian kernel with second moment $\sigma^2 = \Delta^2/12$ as used here, one obtains

$$\phi = \bar{\phi} - \frac{\Delta^2}{24} \nabla^2 \bar{\phi} + \frac{\Delta^4}{1158} \nabla^4 \bar{\phi} + O(\Delta^6) \quad (2.6)$$

Applying the moment expansion to the SGS stress tensor, one finds

$$\tau_{ij} = \frac{\Delta^2}{12} (\nabla_k \bar{u}_i) (\nabla_k \bar{u}_j) + \frac{\Delta^4}{288} (\nabla_k \nabla_l \bar{u}_i) (\nabla_k \nabla_l \bar{u}_j) + \dots \quad (2.7)$$

Retaining just the leading term in the expansion yields the nonlinear/gradient model (NGM) (Clark *et al.* 1979a; Leonard 1975) which has been inferred recently using a data-driven approach (Jakhar *et al.* 2024). With some care, the next-order correction can also be inferred from DNS data (Jakhar *et al.* 2025); we will refer to Equation (2.7) hereon as the NGM4 model. One can also apply the moment expansion to the component tensors and find that $L = O(\delta^2)$, $C = O(\delta^4)$, and $R = O(\delta^6)$, so that L provides the leading-order contribution to τ , with C and R representing progressively smaller corrections. Specifically,

$$\tau = L + C + O(\delta^6). \quad (2.8)$$

Note that carrying out expansions such as (2.6) and (2.7) to higher orders quickly becomes meaningless on a coarse grid due to discretization errors, leading to a loss of accuracy and, ultimately, divergence of the series. Indeed, an LES model including terms up to $O(\delta^6)$, referred to as NGM6, was found to give no improvement in accuracy compared to NGM4 (Jakhar *et al.* 2025). We will discuss this important observation in more detail in subsequent sections.

The coarsest filter scale for which the expansion (2.7) would be expected to yield a reasonable approximation of the SGS stress can be estimated by comparing the magnitude of the two leading terms in the expansion, evaluated using the original rather than the filtered velocity:

$$\ell_i = \left(\frac{\int \langle \left\| \frac{1}{12} (\nabla_k u_i) (\nabla_k u_j) \right\|_F \rangle dt}{\int \langle \left\| \frac{1}{288} (\nabla_k \nabla_l u_i) (\nabla_k \nabla_l u_j) \right\|_F \rangle dt} \right)^{1/2}. \quad (2.9)$$

Here $\|\cdot\|_F$ is the Frobenius norm over tensor indices and $\langle \cdot \rangle$ denotes spatial averaging. For Δ larger than ℓ_i , the series expansion would be expected to diverge and any finite truncation would yield a poor approximation. We will validate this estimate using a variety of *a priori* and *a posteriori* benchmarks below. Defined this way, ℓ_i can be thought of as the integral scale that describes all relevant coherent structures, e.g., vortices and vorticity filaments.

2.3. Physically-informed data-driven equation inference

In order to infer the relevant SGS variables and the associated governing equations from the data, we use the machine learning algorithm SPIDER which leverages group representation theory to generate term libraries, weak formulation of PDEs to replace evaluation of derivatives with numerically well-conditioned quadratures, and fast and efficient sparse regression algorithms for data-driven inference of equivariant physical relations (Gurevich 2025a). The distinguishing feature of SPIDER compared to other sparse regression approaches used for construction of explicit LES models (Jakhar *et al.* 2024, 2025; Zanna & Bolton 2020b) is its systematic and exhaustive approach to defining the search space. One starts by enumerating the irreducible representations of the relevant symmetry group of the problem (here, rotations). Specifically, we consider tensor representations. Furthermore, the relevant differential operators are defined via generators of Lie group actions. Tree tensors of various ranks are constructed using tensor products of these operators acting on all the fields. Finally, a term library \mathcal{L}_m corresponding to a particular irreducible representation m of the full symmetry group (including both continuous

and discrete symmetries, if any) is constructed from contractions of the tree tensors (Golden *et al.* 2023). These formally infinite libraries are made finite by truncation based on complexity (i.e., how many times any field or derivative shows up in a given term). Each such library defines a search space of explicitly equivariant relations in the form

$$c_1 F_1 + \cdots + c_N F_N = 0, \quad (2.10)$$

where $F_n \in \mathcal{L}_m$ and c_n are constant coefficients that need to be determined using properly nondimensionalized training data (Gurevich *et al.* 2024b). Alternatively, to search for constitutive relations defining, say, the SGS stress tensor, one can use an inhomogeneous version of Equation (2.10)

$$F_0 = c_1 F_1 + \cdots + c_N F_N \quad (2.11)$$

where F_0 is a tensor field that may or may not be a part of the library \mathcal{L}_m but transforms according to the same irreducible representation.

Each term in Equation (2.10) or (2.11) is then evaluated in weak form to minimize the effects of noise and discretization, yielding a linear system for the coefficients c_n . One (in the case of Equation (2.11)) or more (in the case of Equation (2.10)) parsimonious relations are then identified for each level of complexity using a greedy regression algorithm (Gurevich 2025a). This whole procedure is automated using a Python-based implementation, PySPIDER (Gurevich 2025b), once the LES variables and their transformation rules under the symmetry have been specified. Note that, for a given dataset, SPIDER yields equations with a single set of numerical coefficients. To capture the dependence of these coefficients on physical parameters such as viscosity ν and filter scale Δ , we repeat the analysis using multiple data sets corresponding to different values of these parameters, which allows discovery of their scaling behavior. Dimensional analysis can be used to further constrain the functional form of the few remaining coefficients c_n that will serve as parameters of the inferred LES model.

3. Results

3.1. Model inference

For each of the three flows, F1, F2, and F3, we begin by applying the Gaussian filtering at a particular scale Δ to fully-resolved DNS solutions and storing the result on a coarse grid with resolution equal to the filter scale (which is equivalent to additionally imposing a sharp spectral filter). We do this for a collection of Δ ranging from ℓ_i down to the DNS grid resolution. We then employ SPIDER to find the parameterization for τ using a rank-2 symmetric trace-free and rank-0 (scalar) libraries constructed using \bar{u}_i and \bar{p} as the variables. Across multiple datasets (corresponding to different flows and filter scales) and in both tensor representations, inhomogeneous regression consistently identifies the leading-order parameterization

$$\tau_{ij} \approx c_1 (\nabla_k \bar{u}_i) (\nabla_k \bar{u}_j) \equiv \tau_{ij}^{(2)}. \quad (3.1)$$

Using dimensional analysis and scaling analysis (i.e., repeated regression over the range of filter scales), we find $c_1 \approx \Delta^2/12$, consistent with the series expansion (2.7). This result corresponds to the NGM model which is known to be deficient; in particular, it incorrectly predicts that the local energy flux $\Pi = -\tau_{ij} \bar{S}_{ij}$ (where \bar{S} is the symmetric part of $\nabla \bar{u}$) vanishes in 2D despite the high correlation between τ and $\tau^{(2)}$ (Jakhar *et al.* 2024). In order to capture higher-order corrections that yield non-vanishing energy flux, we repeat inhomogeneous regression for the difference $\tau - \tau^{(2)}$, reliably finding

$$\tau_{ij} - \tau_{ij}^{(2)} \approx c_2 (\nabla_k \nabla_m \bar{u}_i) (\nabla_k \nabla_m \bar{u}_j) \equiv \tau_{ij}^{(4)}. \quad (3.2)$$

Using dimensional and scaling analysis yields $c_2 \approx \Delta^4/288$, again consistent with the series expansion (2.7). The parameterization $\tau = \tau^{(2)} + \tau^{(4)}$ is the NGM4 model, which is an improvement over NGM that captures some of the local and net energy fluxes (Jakhar *et al.* 2025). However, NGM4 does not provide an accurate prediction for these fluxes, as illustrated by Figure 2.

It is natural to ask whether an even more accurate parameterization can be found in this manner. However, inhomogenous regression does not identify any robust relations between \bar{u}_i , \bar{p} and the difference $\tau - \tau^{(2)} - \tau^{(4)}$. Note that the parameterization $\tau = \tau^{(2)} + \tau^{(4)}$ includes the leading order contributions from L and C but not R , as discussed in subsection 2.2. Therefore, we simply add R itself as the next correction

$$\tau_{ij} = \frac{\Delta^2}{12} (\nabla_k \bar{u}_i) (\nabla_k \bar{u}_j) + \frac{\Delta^4}{288} (\nabla_k \nabla_m \bar{u}_i) (\nabla_k \nabla_m \bar{u}_j) + R_{ij} \quad (3.3)$$

and treat it as an additional LES variable describing the small scales. The introduction of a new tensor variable requires an additional tensor-valued governing equation to close the system. Constructing rank-2 symmetric trace-free and scalar libraries using \bar{u}_i , \bar{p} , R_{ij} as variables and performing homogeneous regression, we robustly find an evolution equation in the form

$$\partial_t R_{ij} = -c_1 \bar{u}_k \nabla_k R_{ij} + c_2 (R_{ik} \nabla_k \bar{u}_j + R_{jk} \nabla_k \bar{u}_i) + c_3 \nabla^2 R_{ij} - c_4 R_{ij} \quad (3.4)$$

across all datasets and both representations, where both yield the same evolution equation with near-identical coefficients, demonstrating consistency across tensor representations. Here R_{ij} is a symmetric tensor; the inferred evolution preserves this symmetry by construction, as rotational and Galilean invariance are enforced directly through the equivariant library construction in SPIDER, rather than imposed *post hoc*. While reminiscent of Reynolds-stress transport models, equation 3.4 is derived entirely from filtered DNS data without phenomenological assumptions or prescribed pressure-strain closures.

We use a combination of dimensional and scaling analysis to identify the parametric dependence of the coefficients. In particular, c_1 and c_2 do not scale with any material parameters, are dimensionless, and have values close to unity; therefore, we set $c_1 = c_2 = 1$. Indeed, this value of c_1 corresponds to the Galilean invariance which we inferred from data rather than assumed at the outset. Similarly, dimensional consistency and numerical scaling show that $c_3 = \nu$.

The coefficient c_4 has units of inverse time and should therefore scale as ν/Δ^2 . However, its numerical values are inconsistent with this scaling: instead, we find $c_4 = O(\omega_{\text{rms}})$. Therefore, we abandon the assumption that c_4 is a constant and consider it to be a scalar function of the LES variables. In this paper, we make the simplifying assumption that c_4 is independent of \bar{p} and R_{ij} . Furthermore, Galilean invariance implies that c_4 can depend only on spatial derivatives of \bar{u}_i . Rotational invariance further implies that c_4 is a function of invariants of the tensors $\nabla_j \bar{u}_i$, $\Delta \nabla_j \nabla_k \bar{u}_i$, etc. In fact, dimensional arguments show that the dominant contribution is a function of invariants of \bar{S} and $\bar{\Omega}$, the symmetric and antisymmetric parts of $\nabla \bar{u}$. Following (Pope 1975), we consider the two invariants $I_1 = 2\bar{S}_{ij}\bar{S}_{ij}$ and $I_2 = 2\bar{\Omega}_{ij}\bar{\Omega}_{ij}$. The Buckingham Pi theorem requires $c_4 = \sqrt{I_1} f(I_1/I_2)$, where $f(\cdot)$ is an arbitrary function. Writing $c_4 = c_{41}\sqrt{I_1} + c_{42}\sqrt{I_2} + c_{43}\sqrt{I_1 + I_2}$ and performing sparse regression on different data sets, we identify the best-fit expression as

$$c_4 = \alpha \sqrt{I_1 + I_2} \equiv \alpha I \quad (3.5)$$

where α is found to be in the range 0.1–0.25 for all training sets. As we show below, this choice yields a fairly accurate description of the training data. However, an even more accurate approximation could, in principle, be inferred using symbolic regression.

We will refer to the combination of equations (3.3) and (3.4) as the NGMR model.

3.2. *A priori* Benchmarks

In order to quantify how accurate the resulting data-driven model is, let us define a magnitude-aware cross-correlation between two tensor fields A and B by

$$\text{CC}(A, B) = \frac{\int \langle A_{ij} \dots B_{ij} \dots \rangle dt}{\max(\int \langle A_{ij} \dots A_{ij} \dots \rangle dt, \int \langle B_{ij} \dots B_{ij} \dots \rangle dt)}. \quad (3.6)$$

While remaining bounded by unity, this definition penalizes magnitude mismatch, providing a stricter measure of the similarity than the standard Pearson correlation. We can now define the accuracy of an LES model in reproducing a tensor field ϕ computed from (filtered) DNS data as

$$\mathcal{A}(\phi) = \text{CC}(\phi^{\text{DNS}}, \phi^{\text{LES}}) \quad (3.7)$$

with $\mathcal{A}(\phi) = 1$ indicating an exact match.

To assess *a priori* performance of our data-driven LES model, we calculate the accuracy of the SGS tensor $\mathcal{A}(\tau)$, the local energy fluxes $\mathcal{A}(\Pi)$, and the ratio of the net energy fluxes $\langle \Pi^{\text{LES}} \rangle / \langle \Pi^{\text{DNS}} \rangle$. These quantities are all computed using filtered DNS data. The results are shown in [Figure 2](#) as a function of the (nondimensional) filter scale δ for each of the three canonical flows F1, F2, and F3. For comparison, we also included the predictions of several other popular LES models: the similarity model, dynamic mixed model, dynamic Smagorinsky model, and NGM4; these are described in [Appendix B](#) and do not include any modifications required for numerical stability. Unsurprisingly, dynamic Smagorinsky fails to predict the SGS stress tensor quantitatively for any δ . The similarity and dynamic mixed model yield reasonable predictions only for $\delta \lesssim 0.1$. NGM4 improves significantly on these LES models but still trails NGMR, which yields near-perfect predictions across all filter scales considered, all the way up to $\Delta = \ell_i$ ($\delta = 1$).

The weakness of the phenomenological LES models becomes even more apparent when one considers the local energy flux Π . No phenomenological models can predict Π even for very small values of δ . On the other hand, NGM4 is found to outperform all of the phenomenological LES models across the entire range filter scales. But the most accurate results are provided by NGMR, which achieves the most accurate results out of all LES models considered; the most noticeable improvement over NGM4 is for the flow F1. Moreover, this is the only model that accurately predicts the flux over the entire range $0 \leq \delta \leq 1$. In contrast, NGM4 exhibits odd drops in the accuracy at low δ for the flows F2 and F3.

Finally, let us consider the predictions for the mean energy flux $\langle \Pi \rangle$. This is a key metric that guides the construction of phenomenological LES models, but despite this, no such model is able to consistently predict the mean flux with even moderate accuracy for any of the 2D flows considered here. NGM4 tends to underpredict the flux by as much as 50% and yields poor predictions for the flow F3 even at very low δ . NGMR is again found to be the most accurate model by a wide margin, yielding consistent predictions for all flows and filter scales considered.

To provide additional illustration of how the five LES models compare, [Figure 3](#) shows the spatial structure of the energy flux Π predicted by the models compared to DNS in a region of the flow F1 denoted by a square box in panel (a). As expected, NGMR predicts the flux essentially perfectly. NGM4 nearly matches DNS in the vorticity-dominated region (top left corner) but fails to accurately capture the width of the filamentary structures in the strain-dominated region. The phenomenological models all struggle to reproduce the spatial structure of the energy flux, which explains the low accuracy shown in the middle row of [Figure 2](#). The pinwheel structures in the top left corner describe “breathing modes” associated with the rotation of elliptic vortices; these co-rotate with the respective vortices. The filamentary structures in the rest of the boxed region represent vortex thinning, the key mechanism for the direct cascade in the extensional regions of the flow. The sign of the flux in this entire region is controlled by the orientation of the vortex

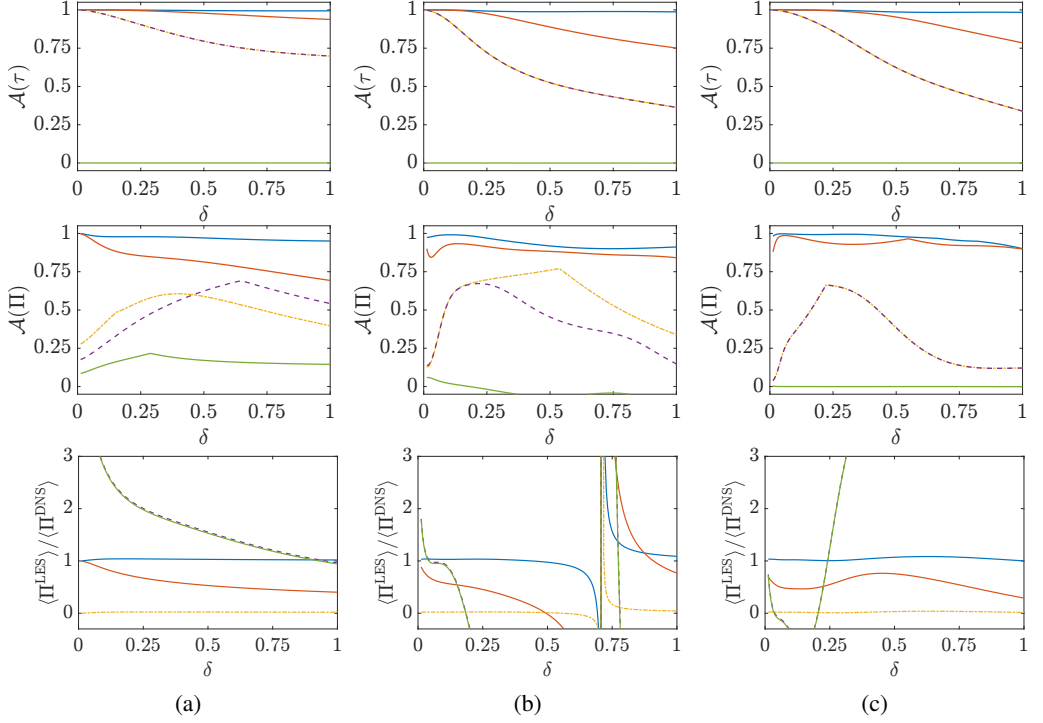


Figure 2: *A priori* benchmarks for the flows F1 (a), F2 (b), and F3 (c) with $\nu = 10^{-5}$: the accuracy of the SGS stress tensor $\mathcal{A}(\tau)$, local energy flux $\mathcal{A}(\Pi)$, and mean energy flux normalized by the DNS value $\langle \Pi^{\text{LES}} \rangle / \langle \Pi^{\text{DNS}} \rangle$. Five LES models are compared: NGMR (blue), NGM4 (orange), similarity (yellow), unclipped dynamic mixed (purple), and unclipped dynamic Smagorinsky (green), each averaged in time over the dataset.

filaments (representing small scales) relative to the extensional direction of the large-scale flow (Reynoso *et al.* 2024) and here is expected to be the same (positive).

Unlike the rest of LES models, NGMR uses an additional variable to describe the subgrid scales and an associated evolution equation (3.4). The accuracy of this equation is quantified in terms of $\mathcal{A}(\partial_t R)$. Here, $\partial_t R_{ij}^{\text{DNS}}$ is computed from snapshots of the fully resolved numerical solution using second-order temporal finite differences, while $\partial_t R_{ij}^{\text{LES}}$ is computed by evaluating the right-hand-side of equation (3.4) using pseudospectral spatial discretization. The results for a range of filter scales are shown in Figure 4. We see that the inferred evolution equation holds to very high accuracy so long as the filter scale is small compared to the size of the coherent structures (δ is small relative to unity).

3.3. Stability and Regularization

LES models typically require regularization in order to keep numerical solutions stable. For example, it is common to perform various averaging procedures or outright clip (set to zero) backscatter contributions for the dynamic mixed model and dynamic Smagorinsky model (Meneveau & Katz 2000a). For the NGMR model, the equation (3.4) has a troubling property that should be addressed to yield well-defined numerical solutions: it is linear and therefore has a scaling symmetry $R \rightarrow sR$ that is not present in the original, nonlinear system (2.1) (where s is any real number). Scaling invariance implies that asymptotic solutions for R depend on the initial conditions and, furthermore, can vanish or explode as the flow evolves. To address these

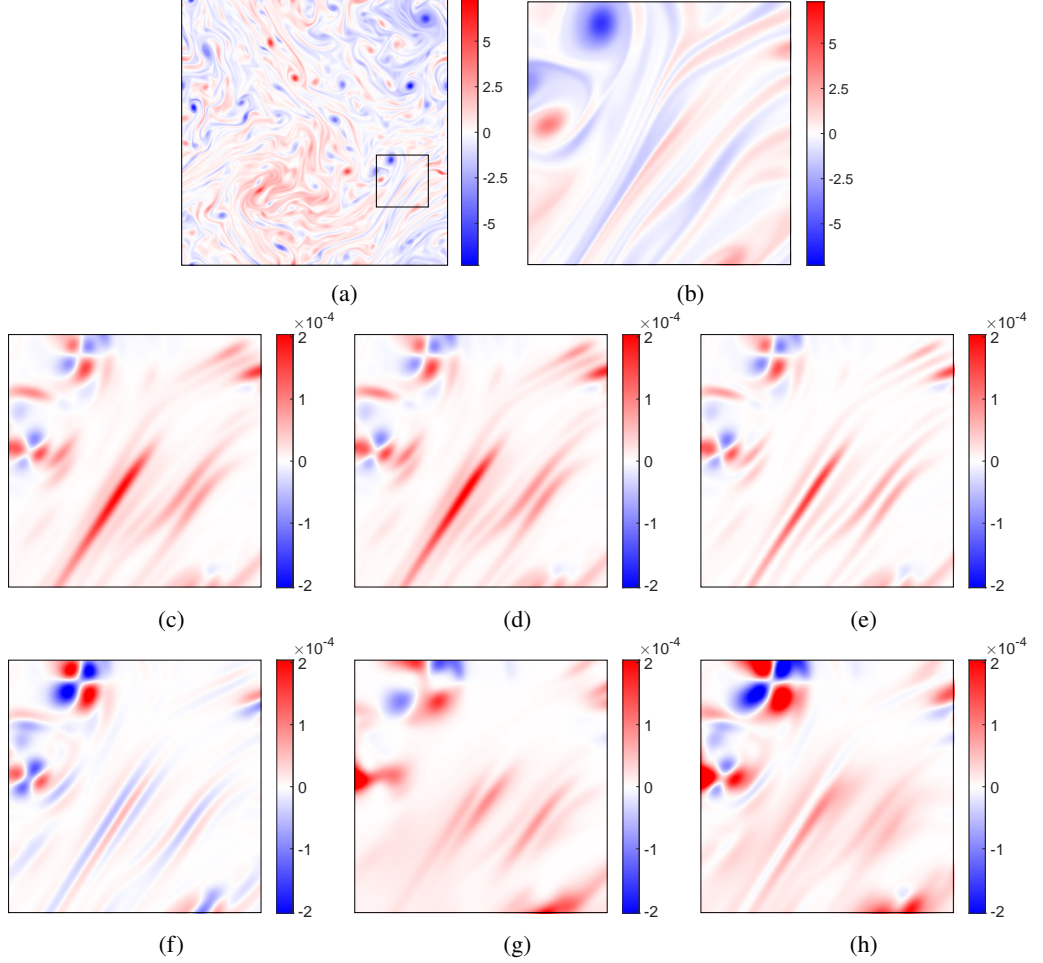


Figure 3: *A priori* energy flux for $\delta = 0.3$ for the state shown in panel (a). The black box delineates the region shown in the remaining panels. Panel (b) shows the details of the vorticity field. The remaining panel show the flux corresponding to (c) FDNS, (d) NGMR, (e) NGM4, (f) similarity model, (g) dynamic Smagorinsky, and (h) dynamic mixed model. The flux is shown without backscatter clipping.

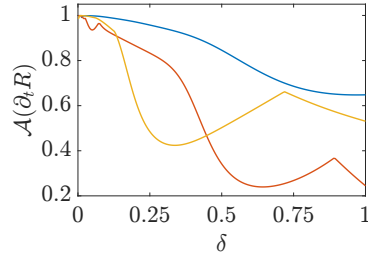


Figure 4: Correlation for the R evolution equation. The datasets correspond to the flows F3 (blue), F2 (orange), and F1 (yellow).

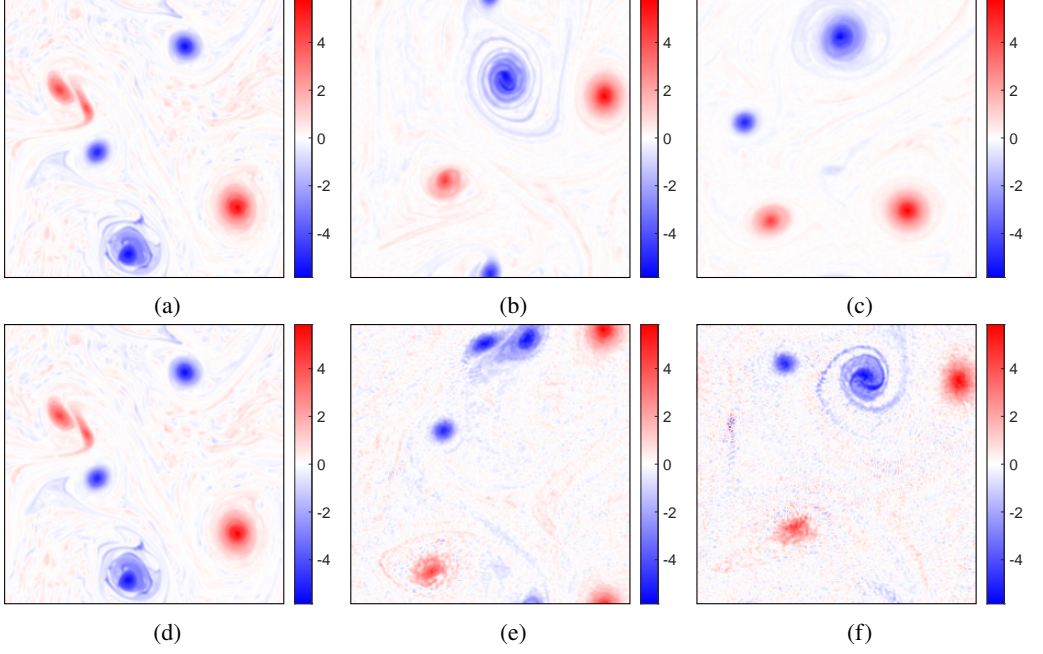


Figure 5: Snapshots of numerical solutions of NGMR for freely decaying turbulence at $\nu = 10^{-7}$ on a 256×256 grid. The vorticity field computed with (a-c) and without (d-f) the regularizing terms (3.11) and (3.12) is shown at $t = 0$ (a,d), $t = 20T_e$ (b,e), and $t = 60T_e$ (c,f).

problems, we separate the Reynolds stress tensor into its traceless part \mathcal{R}_{ij} and the trace k via $R_{ij} = \mathcal{R}_{ij} + \frac{1}{2}k\delta_{ij}$, splitting equation (3.4) into two coupled evolution equations

$$\partial_t \mathcal{R}_{ij} + \bar{u}_l \nabla_l \mathcal{R}_{ij} = \mathcal{R}_{il} \nabla_l \bar{u}_j + \mathcal{R}_{jl} \nabla_l \bar{u}_i - \bar{S}_{lm} \mathcal{R}_{lm} \delta_{ij} + k \bar{S}_{ij} + \nu \nabla^2 \mathcal{R}_{ij} - \alpha I \mathcal{R}_{ij}, \quad (3.8)$$

$$\partial_t k + \bar{u}_i \nabla_i k = 2 \bar{S}_{ij} \mathcal{R}_{ij} + \nu \nabla^2 k - \alpha I k, \quad (3.9)$$

which belong to two different irreducible representations of the rotation group. While this system is formally equivalent to equation (3.4), the decomposition also formally breaks the linearity of equation (3.8) due to the presence of the term $k \bar{S}_{ij}$. However, the decomposed system suffers from similar problems, as the equations have the spurious simultaneous scaling symmetry of \mathcal{R} and k . To completely break the linearity, we replace the evolution equation for the turbulent kinetic energy with the leading order term in its series expansion

$$k = \frac{\Delta^6}{6912} (\nabla_m \nabla^2 \bar{u}_i) (\nabla_m \nabla^2 \bar{u}_i). \quad (3.10)$$

The trace k can be absorbed into the modified pressure and does not contribute to the energy flux. Hence, inaccuracies associated with the spatial discretization or truncation of the expansion do not directly impact the accuracy of the flux predictions. The role of turbulent kinetic energy k is mainly to set the scale for \mathcal{R} as determined by the evolution equation (3.8); this is discussed further in section 4.

A pseudospectral implementation of the resulting LES model yields stable evolution but exhibits some accumulation of energy in the highest wavenumbers, as illustrated in Figure 5. To address this energy build-up, regularization terms are introduced in both the filtered momentum equation and the evolution equation for the Reynolds stress tensor. The functional form of the regularization terms is arbitrary, provided it is dimensionally consistent, transforms appropriately

under the symmetry group, does not considerably impact the dynamics of the large scales, and suppresses the energy build-up. For our pseudospectral implementation, adding a hyperviscous term

$$D_i^{(1)} = \frac{\Delta^5}{20736} (\mathcal{R}_{ij} \mathcal{R}_{ij})^{1/4} \nabla^6 \bar{u}_i = O(\delta^8), \quad (3.11)$$

to the momentum equation and another hyperviscous term

$$D_{ij}^{(2)} = \frac{\Delta^6}{1728} I \nabla^6 \mathcal{R}_{ij} = O(\delta^{12}), \quad (3.12)$$

to the evolution equation for the Reynolds stress tensor is found to be effective while conforming to the constraints outlined above. The corresponding regularized form of the NGMR model suitable for numerical implementation is summarized below:

$$\partial_t \bar{u}_i + \bar{u}_j \nabla_j \bar{u}_i = -\rho^{-1} \nabla_i \bar{p} + \nu \nabla^2 \bar{u}_i - \gamma \bar{u}_i + \bar{f}_i - \nabla_j \tau_{ij} + D_i^{(1)}, \quad (3.13)$$

$$\tau_{ij} = \frac{\Delta^2}{12} (\nabla_k \bar{u}_i) (\nabla_k \bar{u}_j) + \frac{\Delta^4}{288} (\nabla_k \nabla_m \bar{u}_i) (\nabla_k \nabla_m \bar{u}_j) + \mathcal{R}_{ij}, \quad (3.14)$$

$$\partial_t \mathcal{R}_{ij} + \bar{u}_l \nabla_l \mathcal{R}_{ij} = \mathcal{R}_{il} \nabla_l \bar{u}_j + \mathcal{R}_{jl} \nabla_l \bar{u}_i + \nu \nabla^2 \mathcal{R}_{ij} - \bar{S}_{lm} \mathcal{R}_{lm} \delta_{ij} + k \bar{S}_{ij} - \alpha I \mathcal{R}_{ij} + D_{ij}^{(2)}, \quad (3.15)$$

where the turbulent kinetic energy contribution to the SGS stress tensor has been absorbed into the modified pressure. *A posteriori* tests described below show that choosing $\alpha = 1/4$ yields the most accurate predictions.

While the introduction of an additional evolution equation does increase the computational cost of the model compared to, say, NGM4, this cost is more than offset by a very substantial increase in the accuracy, as discussed below. Furthermore, we found that the computational cost of NGMR is comparable to that of other LES models, such as the similarity model.

3.4. *A posteriori* Benchmarks

In order to quantify the accuracy of the online version of the NGMR model and compare it with existing LES methods, we employ a variety of *a posteriori* benchmarks for both freely decaying turbulence and forced turbulence, with and without Rayleigh friction, and over a range of Reynolds numbers and filter scales.

3.4.1. Freely Decaying Turbulence

We start with the analysis of transient flows represented by freely decaying turbulence without Rayleigh friction. Since turbulence disappears too quickly to collect meaningful statistics for one flow realization, we use an ensemble with 12 qualitatively similar but quantitatively distinct initial conditions. All of these initial conditions have roughly the same eddy turnover time T_e , which we will use as a relevant time scale for flow evolution. These initial conditions were constructed using the following procedure: we take the flow F2 shown in Figure 1(b) and add a white noise perturbation at an intermediate wavelength of $k = 24$ with amplitude of $E(k = 24)/5$. The perturbed flow is then evolved for a time interval of about $30T_e$; this procedure is repeated 12 times to yield distinct initial conditions. For each of the 12 initial conditions, DNS is performed for roughly $350T_e$ on a 2048×2048 computational grid for $\nu = 10^{-5}$ and 8192×8192 computational grid for $\nu = 10^{-7}$, ensuring that the dissipation scale is at least 2× larger than the grid scale. The LES solutions are also computed for $250T_e$, with computational grids of resolution 128×128 for $\nu = 10^{-5}$, or 256×256 for 10^{-7} . Representative snapshots of the vorticity field for one of the members of the DNS ensemble are shown in Figure 6 and the movies are provided as Supplementary Material.

For all numerical solutions (both DNS and SGS), we calculate the spatial means of the energy $E = \frac{1}{2} \int_{\Omega} \bar{\mathbf{u}} \cdot \bar{\mathbf{u}} d\mathbf{x}$, enstrophy $H = \frac{1}{2} \int_{\Omega} \bar{\omega}^2 d\mathbf{x}$, energy flux $\Pi_E = \int_{\Omega} \Pi d\mathbf{x}$, and backscatter $\Pi_B =$

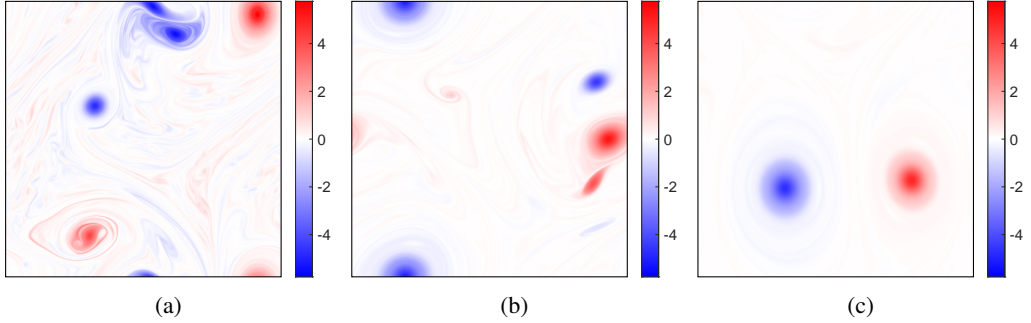


Figure 6: Representative snapshots of the 2048×2048 DNS solution for the freely decaying flow with $\nu = 10^{-5}$ at $t \approx 15T_e$ (a), $t \approx 100T_e$ (b), and $t \approx 250T_e$ (c).

$\int_{\Omega} \Theta(-\Pi) \Pi d\mathbf{x}$, where $\Theta(\cdot)$ is the Heaviside function. The results are shown in Figure 7 for $\nu = 10^{-5}$ and in Figure 8 for $\nu = 10^{-7}$. For both values of viscosity, we find that dynamic Smagorinsky and the mixed model both tend to substantially overestimate the dissipation of energy, which is partially due to the clipping of backscatter required for their stable implementations. NGM4 and the similarity model do better but still underperform considerably compared to NGMR. NGMR also tracks the evolution of enstrophy more accurately than the rest of the models for both values of viscosity, capturing both the overall trend and the quick dips associated with vortex merger events. The dynamic mixed model is again found to be overly dissipative, especially for $\nu = 10^{-5}$. The mean energy fluxes – both net and backscatter – reveal the most dramatic difference between the models. It is only the NGMR model that consistently matches FDNS. All the other models, including NGM4, consistently yield poor predictions throughout the evolution. Most disturbingly, the errors in predicting the overall energy dissipation are particularly severe for the two models—dynamic Smagorinsky and dynamic mixed—designed specifically to predict this quantity.

To compare short-term forecasting, we also define the accuracy metric

$$\mathcal{A}'(\omega) = \frac{\langle \bar{\omega}^{LES} \bar{\omega}^{DNS} \rangle}{\max(\langle \bar{\omega}^{LES} \bar{\omega}^{LES} \rangle, \langle \bar{\omega}^{DNS} \bar{\omega}^{DNS} \rangle)}, \quad (3.16)$$

describing spatial (vs. spatiotemporal, as in the case of equation (3.7)) cross-correlation between an FDNS solution and a corresponding LES solution. The correlation is compared for different models in Figure 9 as a function of time. For the $\nu = 10^{-5}$ case, NGMR yields a solution that remains almost perfectly correlated with DNS for $t/T_e \lesssim 180$ while the correlation for the rest of the models immediately starts to decrease. Interestingly, none of the models can accurately predict the evolution beyond $t/T_e \approx 180$. The results are qualitatively similar for the $\nu = 10^{-7}$ case. Not only does NGMR yield the most accurate solutions for $t/T_e \lesssim 200$, the corresponding solution remains strongly correlated with DNS for a period of time as long as $t/T_e \approx 250$ while, for the rest of the models, the predictions decorrelate completely after $t/T_e \approx 80$.

In addition to accuracy benchmarks, we also qualitatively assess the computational efficiency of our closure. Every model was implemented and benchmarked for around $100T_e$ at multiple grid resolutions ranging from $N_{LES} = 128$ to 1024. All timing tests were performed using naive implementations while ensuring identical numerical schemes, parallelization settings, and hardware configurations to ensure fair comparison. Overall, NGMR performs comparably with all other models, with $NGMR \approx 2$ times faster than dynamic mixed and dynamic Smagorinsky, and ≈ 0.5 times slower than NGM4 and similarity, at the same resolutions.

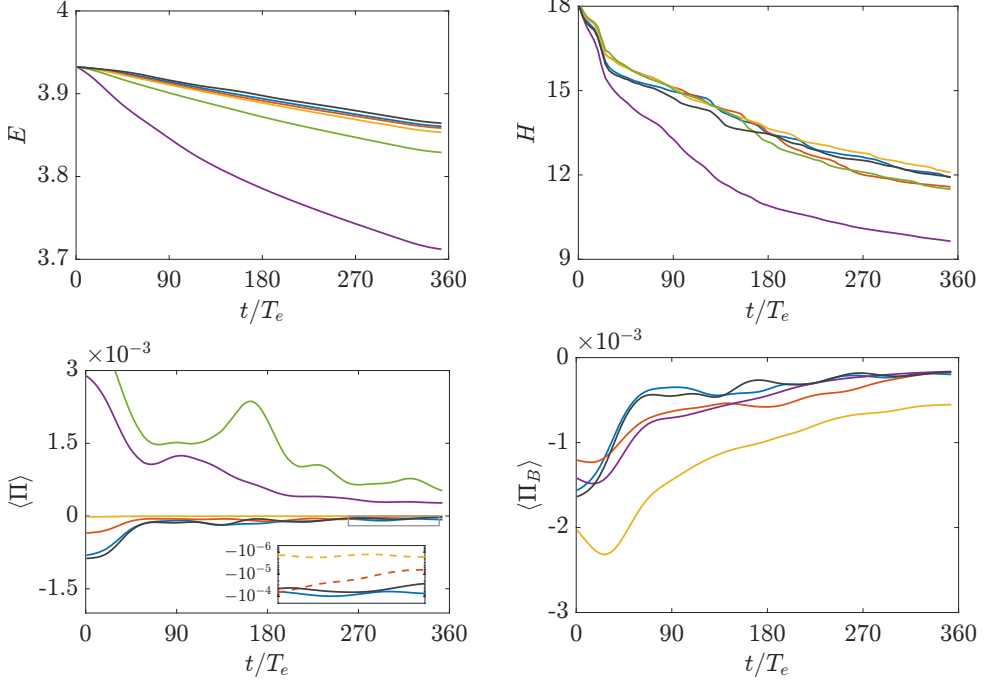


Figure 7: Ensemble averaged *a posteriori* benchmarks for a freely decaying turbulence at $\nu = 10^{-5}$: spatial mean of (a) the energy E , (b) the enstrophy H , (c) the mean energy flux $\langle \Pi_E \rangle$, and (d) the mean backscatter $\langle \Pi_B \rangle$ predicted by LES models and FDNS. Five LES models are compared: NGMR (blue), NGM4 (orange), similarity (yellow), clipped dynamic mixed (purple), and clipped dynamic Smagorinsky (green). The latter two produce no backscatter due to clipping.

3.4.2. Forced Turbulence

Statistically stationary turbulent flows were generated with the forcing profile

$$\nabla \times \mathbf{f} = \frac{1}{2} \sin(k_c x) \sin(k_c y) \quad (3.17)$$

and Rayleigh friction, following Jakhar *et al.* (2025). Note that for this forcing profile, the effective forcing wavelength is given by $k_f = \sqrt{2}k_c$. Representative snapshots of two such flows, labeled F4 and F5, are shown in Figure 10. In both cases, we used a viscosity of $\nu = 10^{-6}$. The flow F4 is forced at wavenumber $k_c = 4$ with Rayleigh friction coefficient $\gamma = 0.05$ and corresponds to $\text{Re} = 2 \times 10^6$. The flow F5 is forced at wavenumber $k_c = 32$ with Rayleigh friction coefficient $\gamma = 10^{-4}$, corresponding to $\text{Re} = 5 \times 10^5$. Rayleigh friction suppresses large-scale condensate formation and, combined with the forcing, yields turbulent flows that are far outside the distribution used for training. As such, F4 will be indicative for testing the generalization of the developed model. Furthermore, Rayleigh friction essentially eliminates intermittency, which can make accurate computation of temporal averages very expensive. The numerical solutions are computed on a 8192^2 grid for DNS to ensure that the dissipation scale is at least $2\times$ larger than the grid scale. We compute LES on different grids ranging from 32^2 – 1024^2 for F4 and one 512^2 grid for the F5 LES models. This resolution corresponds to a nondimensional filter scale $\delta \approx 0.08$ – 2.6 and $\delta \approx 0.23$, for flows F4 and F5 respectively. Because the flows are in a statistically stationary state, we compute time averages of relevant observable quantities from one realization of DNS and the various LES models over $O(10^4)$ eddy turnover times.

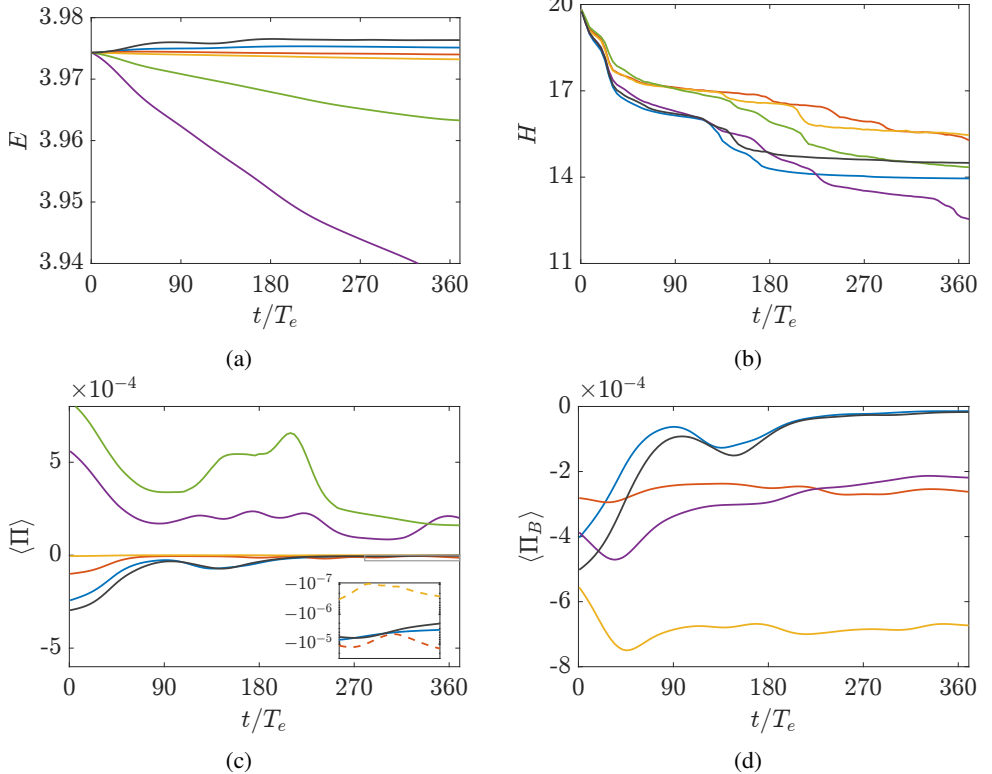


Figure 8: Ensemble averaged *a posteriori* benchmarks for a freely decaying turbulence. The same quantities are shown as in Figure 7 but for $\nu = 10^{-7}$.

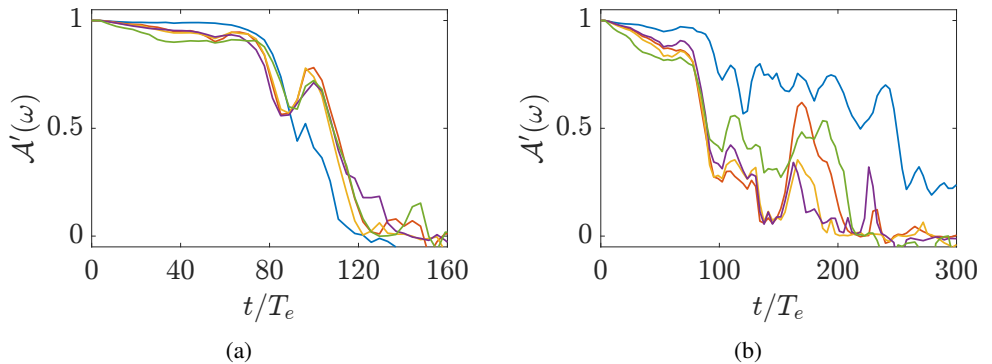


Figure 9: Ensemble average of the cross-correlation $\mathcal{A}'(\omega)$ for the vorticity field of freely decaying turbulence at $\nu = 10^{-5}$ (a) and $\nu = 10^{-7}$ (b). Five models are compared: NGMR (blue), NGM4 (orange), similarity (yellow), clipped dynamic mixed (purple), and clipped dynamic Smagorinsky (green).

To compare the accuracy of different SGS models, we start by computing the time-averaged energy power spectra as well as the probability distribution functions (PDFs) of the pointwise vorticity ω and local SGS energy flux Π for the forced flow F5, which represents the most rigorous and challenging test for any SGS model. This high-Re flow features many small vortices

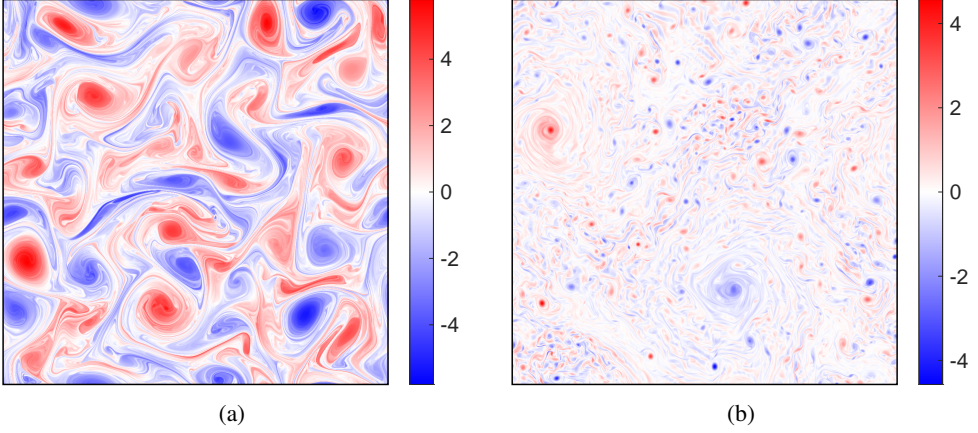


Figure 10: Representative snapshots of the two forced flows F4 (a) and F5 (b) with $\ell_i \approx \ell_d/28$ and $\ell_d/40$, respectively.

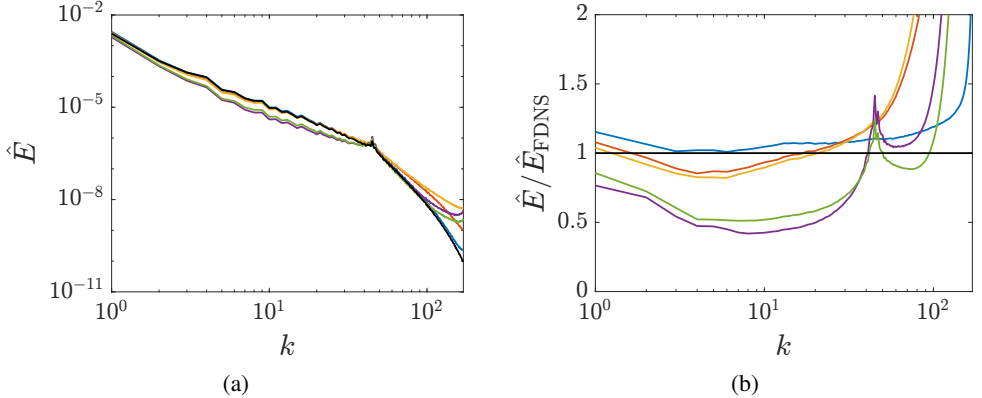


Figure 11: Energy spectrum of the flow F5 (a). FDNS (black) is compared with NGMR (blue), NGM4 (orange), similarity (yellow), clipped dynamic mixed (purple), and clipped dynamic Smagorinsky (green). Respective spectra for each SGS model are normalized by the spectrum of FDNS (b).

with characteristic size determined by the forcing. It also exhibits both the inverse cascade for $k < k_f$ and the direct cascade for $k > k_f$, where $k_f \approx 45$. As Figure 11 illustrates, the dynamic Smagorinsky and the dynamic mixed model both struggle to correctly describe both cascades. This is likely due to the tendency of both models to over-dissipate energy, as we found in the case of freely-decaying turbulence. On the other hand, the similarity model and NGM4 provide an accurate description of the inverse cascade, while providing the least accurate description of the direct cascade. NGMR is the only model capable of accurately predicting the energy spectrum for both cascades. For the vorticity PDFs in figure 12, the dynamic Smagorinsky and the dynamic mixed model provide a reasonably accurate prediction of the central region of the PDF, but fail to describe the tails of the distribution. Similarity and NGM4 is able to noticeably improve matters, as it more accurately captures the tails of the distribution; however they disagree with FDNS everywhere else, particularly in the central, high probability regions. Of the models, NGMR is the only model that is able to accurately describes the entire distribution.

The results describing the energy flux PDF in Figure 13 are perhaps the most interesting.

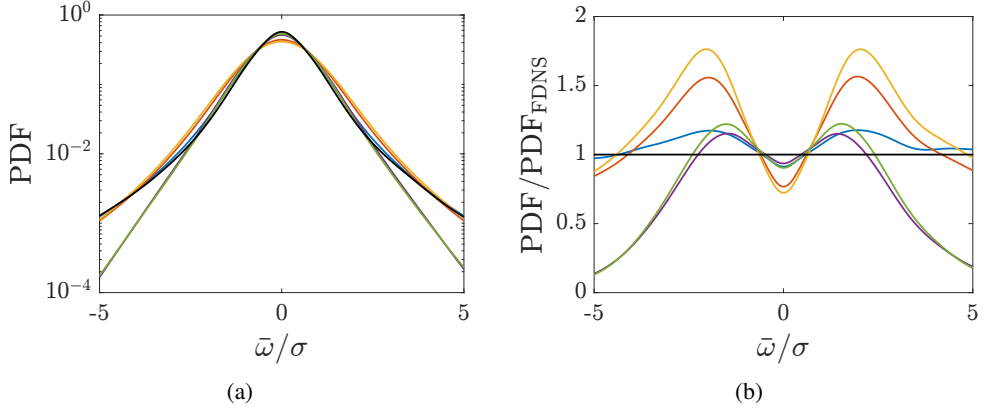


Figure 12: Vorticity PDF for the flow F5 (a). FDNS (black) is compared with NGMR (blue), NGM4 (orange), similarity (yellow), clipped dynamic mixed (purple), and clipped dynamic Smagorinsky (green). PDFs for each SGS model are divided by the PDF of FDNS (b).

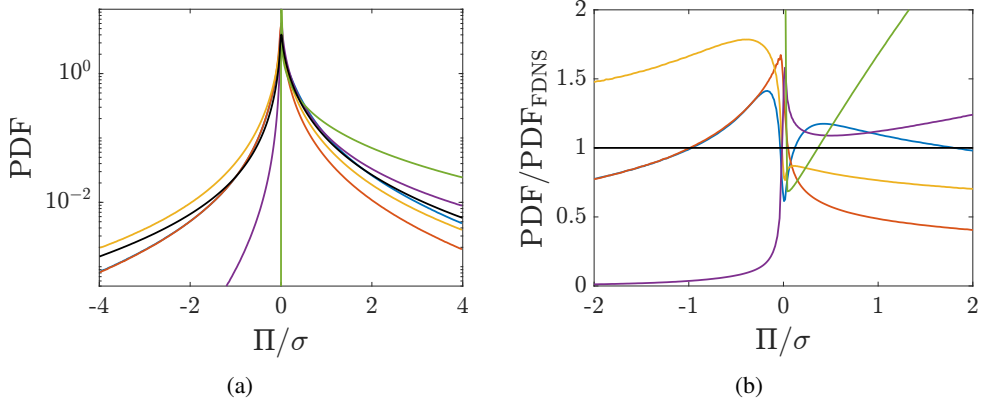


Figure 13: Energy flux PDF for the flow F5 (a). FDNS (black) is compared with NGMR (blue), NGM4 (orange), similarity (yellow), clipped dynamic mixed (purple), and clipped dynamic Smagorinsky (green). PDFs for each SGS model are divided by the PDF of FDNS at the same filter scale (b).

The distribution is found to be asymmetric for DNS, with dissipation ($\Pi > 0$) dominating over backscatter ($\Pi < 0$). This is not unexpected, given that in this flow, the energy is primarily dissipated by regular viscosity at the smallest scales rather than Rayleigh friction at all scales. However, backscatter is quite pronounced, which is a requirement for the inverse cascade. Dynamic Smagorinsky and dynamic mixed model both overestimate dissipation and strongly underestimate backscatter. The similarity model exhibits the opposite trend, underestimating dissipation and overestimating backscatter. The corresponding PDF is nearly symmetric. NGM4 yields a reasonably accurate description of backscatter but strongly underestimates dissipation. Finally, NGMR yields the most accurate prediction of both dissipation and backscatter. These findings are qualitatively consistent with our results for the freely decaying flows.

Having established the superior accuracy of NGMR compared to all the tested models considered here on a variety of benchmarks, we proceed to look for the limits of its applicability. To allow exploration of a wider range of filter scales, we consider the flow F4 forced at a much lower spatial frequency. The *a priori* benchmarks shown in Figure 2 suggest that NGMR can

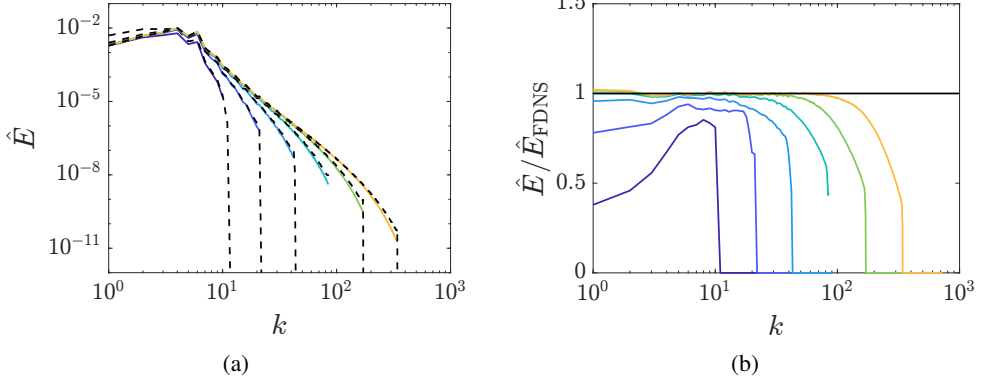


Figure 14: The energy spectrum of the flow F4. The color of the lines (violet to yellow) corresponds to nondimensional filter scales $\delta = \{2.401, 1.314, 0.655, 0.328, 0.082\}$. Respective spectra for each SGS model are normalized by the spectrum of FDNS at the same filter width (b).

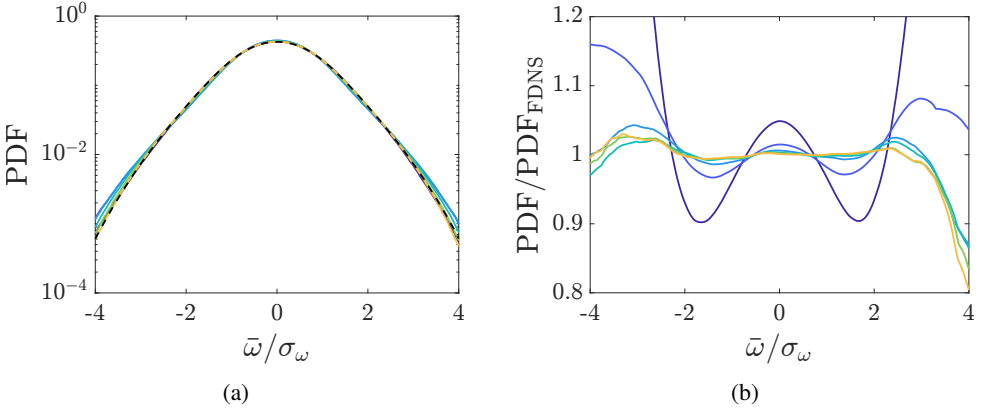


Figure 15: The vorticity PDF for the flow F4 (a). The same color scheme as in Figure 14 is used. Respective PDFs for each SGS model are normalized by the PDF of FDNS at the same filter width (b).

retain accuracy for δ as high as 0.6. To quantify the *a posteriori* accuracy of this model, we compute two metrics, the energy spectrum and the vorticity PDF, for a range of filter scales.

As Figure 14(a) shows, NGMR reproduces the energy spectrum of FDNS almost perfectly for the smallest value of the filter scale. Since no SGS model can describe scales smaller than Δ , as the filter scale increases, a gradual deterioration in the accuracy at high frequencies is expected and indeed observed. Filtering, however, also affects lower frequencies. Hence, to make a more objective comparison between the expected energy spectrum $\hat{E}_{\text{FDNS}}(k)$ and the model prediction $\hat{E}(k)$, we also show their ratio in Figure 14(b), with both spectra computed for the same filter scale. The results demonstrate that NGMR remains accurate up to at least $\delta = 0.328$.

A similar conclusion is made by inspecting the vorticity PDF. Figure 15(a) shows that NGMR reproduces the PDF obtained using FDNS almost perfectly for the smallest value of the filter scale and quite well even for larger values of δ . A more objective measure of accuracy is obtained again by inspecting the ratio of the PDFs for the model and FDNS shown in Figure 15(b). Once again we find that NGMR remains accurate (the ratio stays close to unity) up to at least $\delta = 0.655$. Note that the lack of perfect symmetry as well as the deviation of the ratio from unity at the

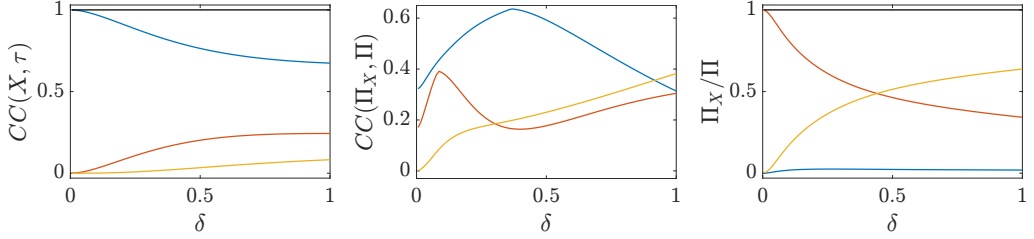


Figure 16: Comparison of the contributions of the different components L, C, R (blue, orange, yellow respectively) in the correlation, local flux, and total flux of the SGS stress tensor for the flow F1. The total contribution of LCR is shown in black.

tails of the distribution at small δ , which can be clearly observed in Figure 15(b), are both due to insufficient statistics rather than model inaccuracy. These deviations are strongly amplified due to the division of one small quantity by another.

4. Discussion

Perhaps one of our most unexpected results is that, according to Figure 2, a model's ability to predict one of the three accuracy benchmarks (SGS stress tensor τ , the local energy flux Π , and the net energy flux) does not imply ability to predict the others. For instance, NGM4 consistently yields high-accuracy predictions for the SGS stress tensor but not the local or net energy flux for $\delta \lesssim 0.25$. A similar statement applies in a stronger form to the similarity and dynamic mixed models for $\delta \lesssim 0.05$. NGMR, on the other hand, yields almost perfect predictions of the net flux even for the range of filter scales where the predicted local flux deviates noticeably from the true profile.

To understand these results, it is helpful to quantify the contribution of the tensors L , C , and R to the SGS stress tensor, the local energy fluxes, and the net energy flux using, respectively, the cross-correlations $CC(X, \tau)$, $CC(\Pi_X, \Pi)$ and the ratio $\langle \Pi_X \rangle / \langle \Pi \rangle$, where $\Pi_X \equiv -X_{ij}\bar{S}_{ij}$ and $X = L, C, R$. Representative results are shown in Figure 16 for flow F1. The dynamic Smagorinsky model fails to predict any of the three quantities with any accuracy for any filter scale, so we will instead focus on the other four models. As expected, we find that the Leonard stress tensor L yields the dominant contribution to τ for $\delta \ll 1$. As δ increases, so do the contributions from C and R , but L still dominates. This is why the similarity and dynamic mixed models, which focus on modeling L and ignore C and R , manage to reproduce τ somewhat well over a range of (small) filter scales, but not for larger δ .

We find the opposite situation for the net energy flux. Here, the contribution of L is negligible for all δ , which explains why the similarity model predicts zero flux and the dynamic mixed model fails to predict the flux with any consistency for all filter scales. It is the C tensor that gives the dominant contribution, which is the reason why NGM4, which models both L and C but not R , captures the net flux well for $\delta \ll 1$. As δ increases, so does the contribution from R , which explains why the predictions of NGM4 quickly deteriorate, while NGMR, which also models R , remains highly accurate. Finally, L , C , and R yield comparable contributions to the local energy fluxes, which is why NGMR is the only model capable of consistently predicting these fluxes over a wide range of filter scales. These results highlight why it is essential to model all three component tensors to predict accurately not only one particular quantity (e.g., net energy dissipation) but a broad collection of physical observables.

Describing backscatter is a difficult challenge that no existing LES model can adequately handle. The *a priori* results presented in Figure 3 seem to suggest that both NGM4 and NGMR can predict backscatter with comparable accuracy. However, our *a posteriori* tests show that the inclusion

of the Reynolds stress tensor into the parameterization of the SGS stress tensor is essential for quantitative accuracy. For freely decaying turbulence, NGMR is the only model whose predicted net backscatter tracks that of FDNS for both values of viscosity. The lower-viscosity case shown in [Figure 8\(d\)](#) is particularly telling: NGMR correctly predicts that backscatter essentially disappears, as it should, when most of the vortices merge to leave a single pair, while all the other models incorrectly predict the net backscatter to asymptote to a nonzero value. In the forced case, the predicted energy flux PDFs for NGMR and NGM4 shown in [Figure 13](#) appear indistinguishable for negative values of Π . A closer inspection shows a noticeable difference at low values of $|\Pi|$. Since the flux PDF is sharply peaked at $\Pi = 0$, this difference is strongly amplified, yielding a substantial improvement in the accuracy for NGMR versus NGM4 as illustrated by, e.g., the energy spectra shown in [Figure 11](#).

While NGM4 is essentially an LES model, the structure of NGMR is distinctly different, with the Reynolds stress tensor R playing the role of a subgrid-scale variable described by its own evolution equation. In this sense, NGMR is more similar to RANS than LES models. Unlike NGMR, most popular RANS models such as the k - ε , k - ω and Spalart-Allmaras model (Wilcox 2008; Chien 1982; Spalart & Allmaras 1992) use one or more scalar fields describing the subgrid scales and rely on the Boussinesq assumption for the SGS stress tensor. Scalar fields are fundamentally incapable of correctly describing inter-scale fluxes, as fluxes crucially depend on the orientation of the small-scale structures; some examples are vorticity filaments in 2D and vortex sheets in 3D relative to the expanding and contracting directions of the large-scale flow. NGMR is closer in form to full-Reynolds-stress models such as Wilcox Stress-omega (Wilcox 2006) and SSG/LRR (Eisfeld *et al.* 2016). These RANS models describe subgrid scales using the Reynolds stress tensor as well as an additional scalar field (ω) related to turbulent kinetic energy, each described by its own evolution equation similar to our equations [\(3.8\)](#) and [\(3.9\)](#). A notable difference is the opposite sign of the production term in the evolution equation for R , which reflects the two-dimensional nature of the flows considered in this study.

We found that a direct parameterization of the turbulent kinetic energy equation in terms of the resolved velocity field using the moment expansion does not significantly hinder the accuracy of our model. However, it is almost certain that the accuracy could be increased further by replacing this parameterization with an evolution equation for k inferred from data which, unlike equation [\(3.9\)](#), would include terms nonlinear in, or independent of, both R and k , which is a requirement for breaking the scale-invariance of the subgrid-scale variables. It is also worth noting that many of the terms in the inferred evolution equation [\(3.4\)](#) (and hence equation [\(3.8\)](#)) can be obtained analytically through the moment expansion of $\partial_t R_{ij}$. The details can be found in [Appendix C](#). In particular, the coefficient $c_1 = 1$ of the advection term is recovered to all orders in σ , reflecting the Galilean symmetry of the problem. We also find, to leading order in σ , the value of two other coefficients: $c_2 = 1$ and $c_3 = \nu$. The formal expansion yields

$$\begin{aligned} \partial_t R_{ij} = & -\bar{u}_l \nabla_l R_{ij} + R_{il} \nabla_l \bar{u}_j + R_{jl} \nabla_l \bar{u}_i + \nu \nabla^2 R_{ij} - \nu \frac{\sigma^6}{2} \nabla_k \nabla_l \nabla^2 \bar{u}_i \nabla_k \nabla_l \nabla^2 \bar{u}_j \\ & + \nabla_k \nabla^2 \bar{u}_i M_{kj} + \nabla_k \nabla^2 \bar{u}_j M_{ki} + \mathcal{O}(\sigma^8) \end{aligned}$$

where M_{ij} is a tensor that cannot be expressed in terms of \bar{p} , \bar{u}_i , and R_{ij} without introducing higher-order derivatives, which were found to be numerically noisy and led to instabilities in practice. Consequently, M_{ij} must also be modeled. The two viscous terms are negligible at high Re and can be ignored. The second viscous term was not picked up by SPIDER not only because our training data did not include lower- Re flows but also because this term is of higher symbolic complexity than we have included in the search space. SPIDER yields a data-driven parameterization for the terms involving M_{ij} that is linear in R_{ij} ; it is this parameterization that limits the accuracy of the evolution equation for the Reynolds stress tensor and consequently the

entire NGMR model at high Re . Finding a better (more accurate and nonlinear) parameterization is a clear target for improving the accuracy of the model further.

Our *a posteriori* results differ considerably from those reported in other studies. For instance, we find a rather significant disagreement between FDNS and NGM4 for both the vorticity PDF and the energy spectra, whereas Jakhar *et al.* (2025) find near-perfect agreement for both metrics. In large part, this is due to the considerably lower values of both Re and δ used in their study, which brings us to the issue of proper model validation procedures. Whatever its stated objective, every LES and RANS model is formulated in terms of a parameterization for the SGS stress tensor. Indeed, in order for a model to accurately predict a variety of physical observables rather than, say, just the energy dissipation rate, an accurate parameterization of τ is essential. The formal moment expansion of τ is expected to converge, yielding such a parameterization, only for $\delta < O(1)$. On the other hand, as our *a priori* benchmarks illustrate, many LES models that yield extremely accurate predictions for $\delta \ll 1$ quickly fall apart as δ increases. Practical considerations dictate that δ be chosen as large as possible, so both *a priori* and *a posteriori* benchmarks should be evaluated for $\delta = O(1)$ to obtain a fair evaluation of a model's accuracy.

The choice of Re is equally important and depends on the choice of δ . There are two separate sources of dissipation in the momentum equation: molecular viscosity characterized by the energy flux $\Pi_v \equiv 2\nu\bar{S}_{ij}\bar{S}_{ij}$ and “eddy viscosity” represented by the SGS energy flux $\Pi = -\bar{S}_{ij}\tau_{ij}$. Their ratio defines the Reynolds number Re_Δ at the filter scale. Testing a SGS model in the limit of $Re_\Delta \ll 1$ can yield highly misleading results. In particular, the stability of a SGS model is highly dependent on the strength of the total dissipation. We found unregularized versions of both NGM4 and the learned correction convolutional neural network model of Kochkov *et al.* (2021) to become numerically unstable at higher Re (corresponding to $Re_\Delta \gg 1$), while the original studies showed no sign of instability at lower Re ($Re_\Delta \ll 1$). Regularization appears to be a necessary ingredient for a wide range of structural and hybrid models. The regularization scheme we adopted was found to perform well for pseudo-spectral discretization. Other discretization schemes might require a different regularization to properly balance efficiency, accuracy and numerical stability.

To properly assess numerical stability, *a posteriori* tests should be conducted for $Re_\Delta > 1$, or preferably even $Re_\Delta \gg 1$, which is, indeed, the intended regime for practical applications of any SGS model. These constraints on Re_Δ and δ apply in equal measure to data-driven model inference, as they ensure that the learned models are sufficiently general, robust, and practically useful. Our training and testing data were generated with constraints on both parameters in mind. **Figure 17** provides a summary of where in the (Re, δ) parameter space our data lie. Both the training data (shown as curves) and testing data (shown as symbols) sample the desired parameter range, $Re_\Delta > 1$ combined with $0 < \delta < 1$, shown as the gray box, quite well. Together with our results, this convincingly illustrates that NGMR retains both accuracy and stability not just over a wide variety of flow regimes but also over a wide variety of parameter regimes, as a general SGS model should.

While the present study is restricted to two-dimensional incompressible turbulent flows, such flows represent an important and nontrivial testbed for subgrid-scale modeling due to the presence of strong backscatter, exposing modeling deficiencies that may have otherwise remained hidden in full three-dimensional settings dominated by forward cascades. Models that perform well in two dimensions must therefore more accurately capture the delicate balance between forward and inverse fluxes of various quantities. Moreover, two-dimensional turbulence is not merely a carefully curated test environment, as two-dimensional flows arise naturally in three-dimensional geometries under a variety of conditions, such as rotating, stratified, and vertically confined systems, which are realized in a variety of geophysical and astrophysical settings. However, despite the physical and practical significance of this setting, the modeling framework introduced here is not intrinsically tied to two-dimensional incompressible flows. The framework generalizes to

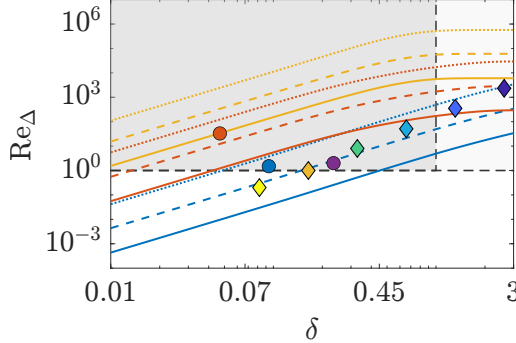


Figure 17: Parameter range for model inference and validation. The gray box represents the parameter region where model inference and validation should be performed. The training data sets F1 (blue), F2 (orange), and F3 (yellow) are shown as curves. The line style corresponds to the value of viscosity $\nu = 10^{-4}$ (solid), $\nu = 10^{-5}$ (dashed) and $\nu = 10^{-6}$ (dot-dashed). The symbols represent the data used for *a posteriori* tests. The circles correspond to the freely decaying flow F2 with $\nu = 10^{-5}$ (blue) and $\nu = 10^{-7}$ (orange) and the forced flow F5 (purple). Diamonds correspond to the forced flow F4 with different filter scales; the same color scheme as in Figure 14 is used.

systems with quadratic nonlinearities, as the structure of the moment expansion and its connection to the Leonards, Cross, and Reynolds tensors carry over. Moreover, the inference of the evolution equation relies on data and symmetries, not on any peculiarities of two-dimensional turbulence. Therefore, extending the present approach to three-dimensional turbulence represents a natural and promising direction for future work.

5. Conclusion

This study shows that, using a combination of formal analysis and physically informed machine learning, it is possible to systematically construct a numerically stable, symbolic, and hence fully interpretable, subgrid-scale model of fluid turbulence. This model requires no adjustable parameters, yet it matches or outperforms state-of-the-art LES models on every single metric, *a priori* or *a posteriori*, for a wide range of two-dimensional, incompressible turbulent flows. Moreover, this model retains accuracy over a much wider range of filter scales and Reynolds numbers. Equally important, the mathematical structure of the model highlights and explains the deficiencies of existing LES models, charting a path towards building even more accurate reduced descriptions of turbulence and other multiscale phenomena in both two and three spatial dimensions. Extension of this model to three-dimensional and/or compressible fluid turbulence is a natural next step.

Acknowledgements. The authors thank Matthew Golden for helpful discussions and insights related to SPIDER and model discovery. This research was supported in part through research cyv resources and services provided by the Partnership for an Advanced Computing Environment (PACE) at the Georgia Institute of Technology, Atlanta, Georgia, USA.

Funding. This work was supported by the Defense Advanced Research Projects Agency (DARPA).

Declaration of Interests. The authors report no conflict of interest.

Data availability statement. The data that support the findings of this study are openly available in GitHub at <https://github.com/cdggjt/jax-cfd-sgs/>

Appendix A. Computational Details & DNS

A.1. Numerical Solver

All DNS simulations were performed using the JAX-CFD framework (Dresdner *et al.* 2023), using a pseudospectral solver for the incompressible 2D Navier–Stokes equation in vorticity–streamfunction formulation on a doubly periodic square domain ($2\pi \times 2\pi$). The full numerical pipeline, including data generation, filtering, and analysis scripts, is available in our open-source repository (Ugliotti & Reynolds 2026). The grid resolution was selected such that it is at least twice as fine (accounting for dealiasing) as the dissipation scale, which corresponds to $\text{Re}_\Delta = 1$. To ensure that numerical solutions are fully resolved, we applied SPIDER to each DNS simulation and verified that the governing equations (continuity and Navier–Stokes) hold to within machine precision. This is essential for data-driven model inference.

The time integration employs a Crank–Nicolson scheme for the viscous terms and a fourth-order Runge–Kutta (RK4) scheme for the nonlinear terms, with the timestep satisfying $\text{CFL} = u_{\max} \Delta t / \Delta x \leq 0.3$ in all simulations. The CFL condition is computed based on the maximum resolved velocity magnitude. The timestep is fixed within each run. All viscous terms are treated implicitly. All computations were performed in double precision to eliminate any potential accumulation of numerical error; single-precision tests yielded quantitatively indistinguishable results. Nonlinear terms were evaluated pseudo-spectrally by computing products in physical space followed by Fourier transformation, with aliasing errors removed using the standard 2/3 truncation rule.

For the *a posteriori* evaluations, each closure scheme was embedded directly into the JAX-CFD solver, which was validated using an equivalent MATLAB implementation that employs an identical numerical scheme. All LES models are solved in the velocity formulation, with a Leray projection used to enforce incompressibility via a spectral pressure projection step. Subgrid-scale terms are treated implicitly wherever numerically feasible and beneficial for stability; remaining terms are treated explicitly.

A.2. Initial Conditions

The *a priori* analysis was performed with DNS data representative of different canonical turbulent regimes generated at $\nu = 10^{-4}, 10^{-5},$ and 10^{-6} using grids of $2048^2, 4096^2,$ and 4096^2 , respectively. The resulting datasets reproduce the expected inertial-range scaling characteristic of two-dimensional turbulence. Zero spatial mean vorticity was enforced in every case. Flows F1 and F3 were initialized from random vorticity fields and evolved under a steady checkerboard forcing (3.17). Each flow was integrated until the total energy reached a statistically stationary state. Flow F1 was forced at an intermediate wavenumber $k_c = 32$, allowing an inverse energy cascade to develop, while still leaving sufficient spectral separation to permit filtering over a wide range of filter scales Δ below the forcing scale. Flow F3 was forced at a low wavenumber $k_c = 4$, allowing a direct cascade to form. Flow F2 was obtained by further evolving flow F1 after turning off the forcing, allowing vortex mergers to proceed and yielding a flow dominated by a small number of large coherent vortices. No linear (Rayleigh) friction, hyperviscosity, or hypoviscosity was used in generating the three initial conditions or any of the nine DNS datasets employed for model inference. The corresponding energy spectra are shown in Figure 18 for the intermediate value of viscosity. Flow F3 features a wide inertial range with a scaling exponent of $\alpha = -4.41$, consistent with expectations (Zhigunov & Grigoriev 2023; Reynolds *et al.* 2024). Flow F2 is transient and displays no inertial range, also as expected. Finally, flow F1 too lacks a clear inertial range due to strong intermittency characteristic of the lack of Rayleigh friction.

Flow F4 is forced at wavenumber $k_c = 4$ with Rayleigh friction with coefficient $\gamma = 0.05$, while flow F5 is forced at wavenumber $k_c = 32$ and includes Rayleigh friction with $\gamma = 10^{-4}$. The initial conditions were generated by evolving both flows until the total energy reached a

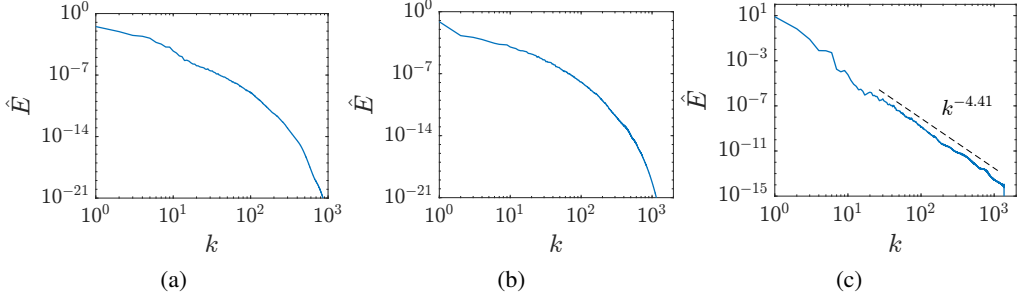


Figure 18: Energy spectrum of the initial condition for DNS at $\nu = 10^{-5}$ of flows F1 (a), F2 (b) and F3 (c).

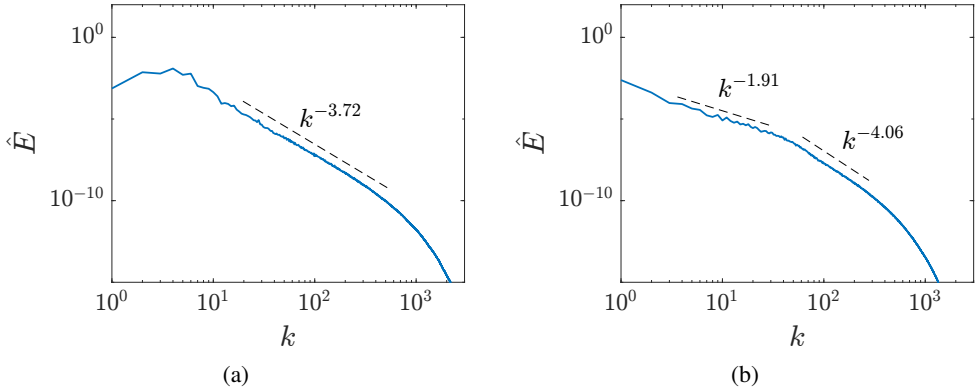


Figure 19: Energy spectrum of the initial condition for DNS of flows F4 (a) and F5 (b).

statistically stationary state. In contrast to the freely decaying flows, both the forcing and friction were maintained while generating the *a posteriori* benchmarking data. The energy spectra of the corresponding initial conditions are shown in Figure 19. Rayleigh friction essentially eliminates intermittency, yielding clean power law scaling for each cascade. Flow F4 exhibits a direct cascade only, with a wide inertial range and scaling exponent of $\alpha = -3.72$. Flow F5 exhibits both an inverse cascade (with scaling exponent $\alpha = -1.91$) and a direct cascade (with scaling exponent $\alpha = -4.06$). These results are again consistent with expectations (Zhu *et al.* 2024). Note that the scaling exponents predicted by the classical Kraichnan–Leigh–Batchelor theory ($\alpha = -5/3$ for the inverse cascade and $\alpha = -3$ for the direct cascade) describe only highly idealized flows with hypo- and hyperviscosity, no Rayleigh friction and, most importantly, no coherent structures.

LES simulations were initialized using the corresponding FDNS solutions and advanced in time using the pseudospectral integration procedure described in subsection A.1. All filtering was performed in Fourier space using a Gaussian filter with second moment $\sigma^2 = \Delta^2/12$, followed by Fourier projection onto the coarse LES grid and combined with 2/3 dealiasing. The filter scale was set at $\Delta = 6\pi/N_{\text{LES}}$, where N_{LES} is the number of grid points in each spatial direction.

Appendix B. LES Models

To evaluate the performance of NGMR, we benchmark it against NGM4 and three representative subgrid-scale (SGS) models most commonly used in large-eddy simulation of incompressible turbulence (Meneveau & Katz 2000b). The selected models span the primary main types of subgrid-scale modeling: functional (Dynamic Smagorinsky), structural (Similarity), hybrid

structural–functional (dynamic Mixed), and gradient-based closures (NGM4). Together, these models thereby provide a representative and increasingly stringent set of baselines for assessing the performance of any new SGS model.

Implementations are identical across the JAX-CFD and MATLAB solvers, and aside from the SGS parameterization itself, all models employ the same numerical discretization, filtering procedures, and timestepping described in Appendix A.1. Spatial derivatives and filtering operations are performed in Fourier space; consequently, derivatives commute exactly with the filter. Each model is summarized below in its canonical formulation following the notation and conventions of Meneveau & Katz (2000b).

Similarity model — The Similarity model (Bardina *et al.* 1980) represents the SGS tensor by the difference between two successive filter levels:

$$\tau_{ij}^{\text{Sim}} = C_{\text{Sim}} \left(\tilde{\bar{u}_i \bar{u}_j} - \tilde{\bar{u}_i \bar{u}_j} \right), \quad (\text{B } 1)$$

where tilde describes a test filter of width $\alpha\Delta$. Following the original formulation of (Bardina *et al.* 1980) we set $C_{\text{Sim}} = \alpha = 1$, making the similarity SGS tensor precisely equal to the standard Leonard stress tensor.

Dynamic Smagorinsky model — The Dynamic Smagorinsky model (Germano *et al.* 1991; Lilly 1992) assumes an eddy-viscosity form for the subgrid stress tensor

$$\tau_{ij}^{\text{DSmag}} = -2\nu_T \bar{S}_{ij}, \quad \nu_T = (C_s \Delta)^2 |\bar{S}|. \quad (\text{B } 2)$$

The Smagorinsky coefficient C_s^2 is computed dynamically from the Germano identity

$$L_{ij} = \tilde{\bar{u}_i \bar{u}_j} - \tilde{\bar{u}_i \bar{u}_j}, \quad (\text{B } 3)$$

where tilde describes a test filter of width $\alpha\Delta$. We follow the convention of $\alpha = 2$ (Germano *et al.* 1991; Lilly 1992). Applying least-squares minimization yields

$$C_s^2 = \frac{L_{ij} M_{ij}}{M_{ij} M_{ij}}, \quad M_{ij} = -2\Delta^2 \left(|\tilde{\bar{S}}| \tilde{\bar{S}}_{ij} - |\bar{S}| \bar{S}_{ij} \right) \quad (\text{B } 4)$$

For our *a posteriori* results, we follow common LES practice by clipping the eddy-viscosity ν_T in order to enforce a positive–definite eddy viscosity, which ensures a purely dissipative baseline model for purposes of stability.

Dynamic mixed model — The Dynamic mixed model (Bardina *et al.* 1980; Zang *et al.* 1993) is a combination of the Dynamic Smagorinsky and Similarity models

$$\tau_{ij}^{\text{DM}} = \tau_{ij}^{\text{Sim}} + \tau_{ij}^{\text{DSmag}} = \tilde{\bar{u}_i \bar{u}_j} - \tilde{\bar{u}_i \bar{u}_j} - 2\nu_T \bar{S}_{ij}, \quad (\text{B } 5)$$

where $\nu_T = (C_s \Delta)^2 |\bar{S}|$ is obtained from the dynamic procedure described previously. We again employ clipping of ν_T in all of our *a posteriori* simulations.

NGM4 — This fourth-order nonlinear gradient model (Jakhar *et al.* 2025) corresponds to the truncation of the moment expansion of τ at fourth order in Δ :

$$\tau_{ij}^{\text{NGM4}} = \frac{\Delta^2}{12} (\nabla_k \bar{u}_i) (\nabla_k \bar{u}_j) + \frac{\Delta^4}{288} (\nabla_k \nabla_m \bar{u}_i) (\nabla_k \nabla_m \bar{u}_j) \quad (\text{B } 6)$$

The first term corresponds to the second–order nonlinear gradient model, also known as the Clark model (Jakhar *et al.* 2024; Clark *et al.* 1979a). NGM4 is of particular interest because it represents NGMR without the Reynolds stress tensor R_{ij} .

Appendix C. Evolution equation for the Reynolds stress tensor

This section discusses the analytical derivation of the evolution equation for the Reynolds stress tensor R . In the continuum limit, this tensor can be approximated well with the moment expansion

$$R_{ij} = \sum_{n=1} c_n \sigma^{2n} (D_n^a \bar{u}_i) (D_n^a \bar{u}_j), \quad (\text{C } 1)$$

where $D_n^a = \partial_\alpha \partial_\beta \cdots \partial_\omega$ is a tensorial differential operator, n indicates its order, a is a shorthand multi-index, and $\sigma^2 = \Delta^2/12$. To leading order in σ ,

$$R_{ij} = \frac{\sigma^6}{4} (\nabla_k \nabla^2 \bar{u}_i) (\nabla_k \nabla^2 \bar{u}_j) + O(\sigma^8). \quad (\text{C } 2)$$

Taking the time derivative, we find

$$\partial_t R_{ij} = \frac{\sigma^6}{4} (\nabla_k \nabla^2 \bar{u}_i) (\nabla_k \nabla^2 \partial_t \bar{u}_j) + \text{Sym.}, \quad (\text{C } 3)$$

where ‘‘Sym.’’ denotes term(s) required to make the expression on the right-hand side symmetric in the indices i and j . Substituting equation (2.3) yields

$$\partial_t R_{ij} = \frac{\sigma^6}{4} (\nabla_k \nabla^2 \bar{u}_i) \nabla_k \nabla^2 \left(-\bar{u}_l \nabla_l \bar{u}_j - \nabla_j \bar{p} + \nu \nabla^2 \bar{u}_j + \nabla_l \tau_{lj} \right), \quad (\text{C } 4)$$

where the last term involving the subgrid stress tensor is higher-order in σ and can be ignored. Collecting terms and using the filtered pressure-Poisson equation to remove the dependence on \bar{p} , we obtain

$$\partial_t R_{ij} = \frac{\sigma^6}{4} \nabla_k \nabla^2 \bar{u}_i \left[\nabla_k \nabla_j (\nabla_l \bar{u}_m \nabla_m \bar{u}_l) - \nabla_k \nabla^2 (\bar{u}_l \nabla_l \bar{u}_j) + \nu \nabla^4 \bar{u}_j \right] + \text{Sym.} + O(\sigma^8). \quad (\text{C } 5)$$

Using the tensor identity (which is only valid in 2D)

$$(\nabla_k \partial_\alpha (\nabla_i u_\beta - \partial_\beta u_i)) (\partial_\beta u_\alpha) = (\nabla_k \nabla^2 u_\beta) (\partial_\beta u_i), \quad (\text{C } 6)$$

one can rewrite the series in terms of R_{ij} by using equation (C 2) one more time, yielding

$$\partial_t R_{ij} = -\bar{u}_l \nabla_l R_{ij} + R_{il} \nabla_l \bar{u}_j + R_{jl} \nabla_l \bar{u}_i + \nu \nabla^2 R_{ij} - \nu \frac{\sigma^6}{2} \nabla_k \nabla_l \nabla^2 \bar{u}_i \nabla_k \nabla_l \nabla^2 \bar{u}_j \quad (\text{C } 7)$$

$$+ \nabla_k \nabla^2 \bar{u}_i M_{kj} + \nabla_k \nabla^2 \bar{u}_j M_{ki} + O(\sigma^8), \quad (\text{C } 8)$$

where the tensor

$$M_{kj} = \frac{\sigma^6}{4} \left[2 \nabla_k \nabla_l \bar{u}_m \nabla_j \nabla_m \bar{u}_l - \nabla^2 \bar{u}_l \nabla_k \nabla_l \bar{u}_j - \nabla_k \bar{u}_l \nabla^2 \nabla_l \bar{u}_j - 2 \nabla_k \nabla_m \bar{u}_l \nabla_l \nabla_m \bar{u}_j \right] + O(\sigma^8) \quad (\text{C } 9)$$

cannot be expressed in terms of R_{ij} .

Equation (C 9) contains the skeleton of the model inferred using our data-driven approach. The formal moment expansion also allows one to systematically identify which terms in the model (3.13) are responsible for its limited accuracy by retaining higher-order terms. In this case, one finds that the advective term $\bar{u}_l \nabla_l R_{ij}$ persists at all orders. The production term $R_{il} \nabla_l \bar{u}_j + R_{jl} \nabla_l \bar{u}_i$ also persists at all orders but enters the evolution equation (3.4) with sign opposite to that found in classical RANS models (Chou 1945). This is because, to leading order, the production term combines the contributions from both the advection term (with the prefactor of -1) and the pressure term (with the prefactor of $+2$) in the momentum equation. The viscous term $-\nu \frac{\sigma^6}{2} \nabla_k \nabla_l \nabla^2 \bar{u}_i \nabla_k \nabla_l \nabla^2 \bar{u}_j$ becomes negligibly small at high Re , so the largest contribution to the error of the evolution equation (3.4), and hence (3.8), is associated with the $O(\sigma^6)$ terms

$\nabla_k \nabla^2 \bar{u}_i M_{kj}$ and $\nabla_k \nabla^2 \bar{u}_j M_{ki}$ that require modeling, making their sum the most suitable candidate for further model improvement.

REFERENCES

BARDINA, J., FERZIGER, J. H. & REYNOLDS, W. C. 1980 Improved subgrid-scale models for large-eddy simulation. *AIAA Journal* **18** (11), 1275–1283.

BECK, A., FLAD, D. & MUNZ, C. 2019 Deep neural networks for data-driven les closure models. *Journal of Computational Physics* **398**, 108910.

BOLTON, T. & ZANNA, L. 2019 Applications of deep learning to ocean data inference and subgrid parameterization. *Journal of Advances in Modeling Earth Systems* **11** (1), 376–399.

CHIEN, KUEI-YUAN 1982 Predictions of channel and boundary-layer flows with a low-reynolds-number turbulence model. *AIAA Journal* **20** (1), 33–38.

CHOU, P. YO 1945 On velocity correlations and the solutions of the equations of turbulent fluctuation. *Quarterly of applied mathematics* **3** (1), 38–54.

CLARK, R. A., FERZIGER, J. H. & REYNOLDS, W. C. 1979a Evaluation of subgrid-scale models using an accurately simulated turbulent flow. *Journal of fluid mechanics* **91** (1), 1–16.

CLARK, ROBERT A., FERZIGER, JOEL H. & REYNOLDS, W. C. 1979b Evaluation of subgrid-scale models using an accurately simulated turbulent flow. *Journal of Fluid Mechanics* **91** (1), 1–16.

DRESDNER, GIDEON, KOCHKOV, DMITRII, NORGAARD, PETER, ZEPEDA-NÚÑEZ, LEONARDO, SMITH, JAMIE A., BRENNER, MICHAEL P. & HOYER, STEPHAN 2023 Learning to correct spectral methods for simulating turbulent flows , arXiv: 2207.00556.

EISFELD, BERNHARD, RUMSEY, CHRISTOPHER L. & TOGIDI, VASSILIOS 2016 Verification and validation of a second-moment-closure model. *AIAA Journal* **54** (5), 1524–1541.

FREZAT, H., BALARAC, G., LE, J., FABLET, R. & LGUENSAT, R. 2021 Physical invariance in neural networks for subgrid-scale scalar flux modeling. *Physical Review Fluids* **6** (2), 024607.

GERMANO, M. 1986 A proposal for a redefinition of the turbulent stresses in the filtered Navier–Stokes equations. *The Physics of Fluids* **29** (7), 2323–2324.

GERMANO, MASSIMO, PIOMELLI, UGO, MOIN, PARVIZ & CABOT, WILLIAM H. 1991 A dynamic subgrid-scale eddy viscosity model. *Physics of Fluids A: Fluid Dynamics* **3** (7), 1760–1765.

GOLDEN, MATTHEW, GRIGORIEV, ROMAN O., NAMBISAN, JYOTHISHRAJ & FERNANDEZ-NIEVES, ALBERTO 2023 Physically informed data-driven modeling of active nematics. *Science Advances* **9** (27), eabq6120.

GUAN, YIFEI, CHATTOPADHYAY, ASHESH, SUBL, ADAM & HASSANZADEH, PEDRAM 2022 Stable a posteriori les of 2d turbulence using convolutional neural networks: Backscattering analysis and generalization to higher re via transfer learning. *Journal of Computational Physics* **458**, 111090.

GUAN, YIFEI, SUBL, ADAM, CHATTOPADHYAY, ASHESH & HASSANZADEH, PEDRAM 2023 Learning physics-constrained subgrid-scale closures in the small-data regime for stable and accurate les. *Physica D: Nonlinear Phenomena* **443**, 133568.

GUREVICH, DANIEL 2025a Data-driven inference of symmetry-equivariant models of natural phenomena. PhD thesis, Princeton University.

GUREVICH, DANIEL 2025b Pyspider: Generalized sparse regression for continuous and discrete data. <https://github.com/sibirica/PySPIDER>.

GUREVICH, D. R., GOLDEN, M. R., REINBOLD, P. A. K. & GRIGORIEV, R. O. 2024a Learning fluid physics from highly turbulent data using sparse physics-informed discovery of empirical relations (spider). *Journal of Fluid Mechanics* **996**, A25.

GUREVICH, DANIEL R., GOLDEN, MATTHEW R., REINBOLD, PATRICK A. K. & GRIGORIEV, ROMAN O. 2024b Learning fluid physics from highly turbulent data using sparse physics-informed discovery of empirical relations (SPIDER). *Journal of Fluid Mechanics* **996**, A25.

JAKHAR, KARAN, GUAN, YIFEI & HASSANZADEH, PEDRAM 2025 An analytical and ai-discovered stable, accurate, and generalizable subgrid-scale closure for geophysical turbulence. *arXiv preprint arXiv:2509.20365*.

JAKHAR, KARAN, GUAN, YIFEI, MOJGANI, RAMBOD, CHATTOPADHYAY, ASHESH & HASSANZADEH, PEDRAM 2024 Learning closed-form equations for subgrid-scale closures from high-fidelity data: Promises and challenges. *Journal of Advances in Modeling Earth Systems* **16** (7), e2023MS003874.

KARPOV, PLATON I., HUANG, CHENGKUN, SITDIKOV, ISKANDAR, FRYER, CHRIS L., WOOSLEY, STAN & PILANIA, GHANSHYAM 2022 Physics-informed machine learning for modeling turbulence in supernovae. *The Astrophysical Journal* **940** (1), 26.

KOCHKOV, DMITRII, SMITH, JAMIE A, ALIEVA, AYYA, WANG, QING, BRENNER, MICHAEL P & HOYER, STEPHAN 2021 Machine learning–accelerated computational fluid dynamics. *Proceedings of the National Academy of Sciences* **118** (21), e2101784118.

LEONARD, ANTHONY 1975 Energy cascade in large-eddy simulations of turbulent fluid flows. In *Advances in geophysics*, , vol. 18, pp. 237–248. Elsevier.

LILLY, D. K. 1992 A proposed modification of the Germano subgrid-scale closure method. *Physics of Fluids A: Fluid Dynamics* **4** (3), 633–635.

LING, JULIA, JONES, REESE & TEMPLETON, JEREMY 2016 Machine learning strategies for systems with invariance properties. *Journal of Computational Physics* **318**, 22–35.

MAULIK, ROMIT, SAN, OMER, RASHEED, ADIL & VEDULA, PRAKASH 2019 Subgrid modelling for two-dimensional turbulence using neural networks. *Journal of Fluid Mechanics* **858**, 122–144.

MENEVEAU, CHARLES & KATZ, JOSEPH 2000a Scale-Invariance and Turbulence Models for Large-Eddy Simulation. *Annual Review of Fluid Mechanics* **32** (Volume 32, 2000), 1–32.

MENEVEAU, CHARLES & KATZ, JOSEPH 2000b Scale-invariance and turbulence models for large-eddy simulation. *Annual Review of Fluid Mechanics* **32** (1), 1–32.

MOSER, ROBERT D., HAERING, SIGFRIED W. & YALLA, GOPAL R. 2021 Statistical Properties of Subgrid-Scale Turbulence Models. *Annual Review of Fluid Mechanics* **53** (1), 255–286.

PAWAR, SURAJ, SAN, OMER, RASHEED, ADIL & VEDULA, PRAKASH 2023 Frame invariant neural network closures for kraichnan turbulence. *Physica A: Statistical Mechanics and its Applications* **609**, 128327.

PEDERSEN, CHRISTIAN, ZANNA, LAURE, BRUNA, JOAN & PEREZHOGIN, PAVEL 2023 Reliable coarse-grained turbulent simulations through combined offline learning and neural emulation. *arXiv preprint arXiv:2307.13144*.

POPE, S. B. 1975 A more general effective-viscosity hypothesis. *Journal of Fluid Mechanics* **72** (2), 331–340.

POPE, STEPHEN B. 2000 Turbulent Flows. ISBN: 9780511840531.

REISSMANN, MAXIMILIAN, HASLBERGER, JOSEF, SANDBERG, RICHARD D & KLEIN, MARKUS 2021 Application of gene expression programming to a-posteriori les modeling of a taylor green vortex. *Journal of Computational Physics* **424**, 109859.

REYNOSO, MATEO, ZHIGUNOV, DMITRIY & GRIGORIEV, ROMAN O 2024 Self-similarity and the direct (enstrophy) cascade in forced two-dimensional fluid turbulence. *Journal of Fluid Mechanics* **995**, A4.

ROSS, ANDREW, LI, ZIWEI, PEREZHOGIN, PAVEL, FERNANDEZ-GRANDA, CARLOS & ZANNA, LAURE 2023 Benchmarking of machine learning ocean subgrid parameterizations in an idealized model. *Journal of Advances in Modeling Earth Systems* **15** (1), e2022MS003258.

SAGAUT, P. & MENEVEAU, CHARLES 2006 *Large Eddy Simulation for Incompressible Flows: An Introduction*. Berlin, Heidelberg: Springer.

SCHMELZER, MARTIN, DWIGHT, RICHARD & CINNELLA, PAOLA 2018 Data-driven deterministic symbolic regression of nonlinear stress-strain relation for rans turbulence modelling. In *2018 Fluid Dynamics Conference*, p. 2900.

SMAGORINSKY, JOSEPH 1963 General circulation experiments with the primitive equations: I. the basic experiment. *Monthly weather review* **91** (3), 99–164.

SPALART, P. & ALLMARAS, S. 1992 A one-equation turbulence model for aerodynamic flows. In *30th Aerospace Sciences Meeting and Exhibit*. American Institute of Aeronautics and Astronautics.

UGLIOTTI, MATTEO & REYNOSO, MATEO 2026 An extension of jax-cfd framework for data-driven closure modeling. <https://github.com/cdggt/jax-cfd-sgs>.

VREMAN, BERT, GEURTS, BERNARD & KUERTEN, HANS 1994 Realizability conditions for the turbulent stress tensor in large-eddy simulation. *Journal of Fluid Mechanics* **278**, 351–362.

VREMAN, BERT, GEURTS, BERNARD & KUERTEN, HANS 1996 Large-eddy simulation of the temporal mixing layer using the Clark model. *Theoretical and Computational Fluid Dynamics* **8** (4), 309–324.

VREMAN, BERT, GEURTS, BERNARD & KUERTEN, HANS 1997 Large eddy simulation of the turbulent mixing layer. *Journal of Fluid Mechanics* **339**, 357–390.

WEATHERITT, JACK & SANDBERG, RICHARD D 2017 The development of algebraic stress models using a novel evolutionary algorithm. *International Journal of Heat and Fluid Flow* **68**, 298–318.

WILCOX, DAVID C. 2006 *Turbulence Modeling for CFD*, 3rd edn. La Canada, CA: DCW Industries, Inc.

WILCOX, DAVID C 2008 Formulation of the $k-\omega$ turbulence model revisited. *AIAA journal* **46** (11), 2823–2838.

ZANG, THOMAS A., STREET, ROBERT L. & KOSEFF, JEFFREY R. 1993 A dynamic mixed subgrid-scale model

and its application to turbulent recirculating flows. *Physics of Fluids A: Fluid Dynamics* **5** (12), 3186–3196.

ZANNA, LAURE & BOLTON, THOMAS 2020a Data-driven equation discovery of ocean mesoscale closures. *Geophysical Research Letters* **47** (17), e2020GL088376.

ZANNA, LAURE & BOLTON, THOMAS 2020b Data-Driven Equation Discovery of Ocean Mesoscale Closures. *Geophysical Research Letters* **47** (17), e2020GL088376, eprint: <https://agupubs.onlinelibrary.wiley.com/doi/pdf/10.1029/2020GL088376>.

ZHIGUNOV, DMITRIY & GRIGORIEV, ROMAN O 2023 Exact coherent structures in fully developed two-dimensional turbulence. *Journal of Fluid Mechanics* **970**, A18.

ZHU, HANG-YU, XIE, JIN-HAN & XIA, KE-QING 2024 Flow patterns and energy spectra in forced quasi-two-dimensional turbulence: effect of system size and damping rate. *Journal of Fluid Mechanics* **996**, A39.